IRAQI JOURNAL OF APPLIED PHYSICS

The *Iraqi Journal of Applied Physics (IJAP)* is a peer reviewed journal of high quality devoted to the publication of original research papers from applied physics and their broad range of applications. IJAP publishes quality original research papers, comprehensive review articles, survey articles, book reviews, dissertation abstracts in physics and its applications in the broadest sense. It is intended that the journal may act as an interdisciplinary forum for Physics and its applications. Innovative applications and material that brings together diverse areas of Physics are particularly welcome. Review articles in selected areas are published from time to time. It aims to disseminate knowledge; provide a learned reference in the field; and establish channels of communication between academic and research experts, policy makers and executives in industry, commerce and investment institutions. IJAP is a quarterly specialized periodical dedicated to publishing original papers, letters and reviews in: Applied & Nonlinear Optics, Applied Mechanics & Thermodynamics, Digital & Optical Communications, Electronic Materials & Devices, Laser Physics & Applications, Plasma Physics & Applications, Quantum Physics & Spectroscopy, Semiconductors & Optoelectronics, Solid State Physics & Applications, Alternative & Renewable Energy, and Environmental Science & Technology.

ISSN (Print): 1813-2065, ISSN (Online): 2309-1673, ISSN (Letters): 1999-656X

EDITORIAL BOARD

Editorial Office:
P. O. Box 55259, Baghdad 12001, IRAQ
Website: www.iraqiphysicsjournal.com
Emails: info@iraqiphysicsjournal.com, editor_ijap@yahoo.co.uk, ijap.editor@gmail.com,

ADVISORY BOARD

SPONSORED AND PUBLISHED BY
THE IRAQI SOCIETY FOR ALTERNATIVE AND RENEWABLE ENERGY SOURCES & TECHNIQUES (I.S.A.R.E.S.T.)

IRAQI JOURNAL OF APPLIED PHYSICS

ISSN (Print): 1813-2065, ISSN (Online): 2309-1673, ISSN (Letters): 1999-656X

INSTRUCTIONS TO AUTHORS

CONTRIBUTIONS

Contributions to be published in this journal should be original research works, i.e., those not already published or submitted for publication elsewhere, individual papers or letters to editor.
Manuscripts should be submitted to the editor at the mailing address:
Iraqi Journal of Applied Physics, Editorial Board, P. O. Box 55259, Baghdad 12001, IRAQ
Website: www.iraqiphysicsjournal.com
Email: editor@iraqiphysicsjournal.com, editor_ijap@yahoo.co.uk, ijap.editor@gmail.com

MANUSCRIPTS

Two hard copies with soft Word copy on a CD or DVD should be submitted to Editor in the following configuration:

- **One-column** Double-spaced one-side A4 size with 2.5 cm margins of all sides
- Times New Roman font (16pt bold for title, 14pt bold for names, 12pt bold for headings, 12pt regular for text)
- Manuscripts presented in English only are accepted.
- English abstract not exceed 150 words
- 4 keywords (at least) should be maintained on (PACS preferred)
- Author(s) should express all quantities in SI units
- Equations should be written in equation form (*italic* and symbolic) NOT in plain text
- Tables and Figures should be separated from text and placed in new pages after the references
- Charts should be indicated by the software used for generating them (e.g., Excel, MATLAB, Grapher, etc.)
- Figures and diagrams can be submitted in original colored forms for assessment and they will be returned to authors after provide printable copies
- Only original or high-resolution scanner photos are accepted
- For electronic submission, articles should be formatted with MS-Word software.

AUTHOR NAMES AND AFFILIATIONS

It is IJAP policy that all those who have participated significantly in the technical aspects of a paper be recognized as co-authors or cited in the acknowledgments. In the case of a paper with more than one author, correspondence concerning the paper will be sent to the first author unless staff is advised otherwise.
Author name should consist of first name, middle initial, last name. The author affiliation should consist of the following, as applicable, in the order noted:
- Company or college (with department name or company division), Postal address, City, Governorate or State, zip code, Country name, contacting telephone number, and e-mail

REFERENCES

The references should be brought at the end of the article, and numbered in the order of their appearance in the paper. The reference list should be cited in accordance with the following examples:
[1] X. Ning, R. Benford and M.R. Lovell, "On the Sliding Friction Characteristics of Unidirectional Continuous FRP Composites", *J. Tribol. Func. Mater.*, 124(1) (2002) 5-13.
[2] M. Barnes, "Stresses in Solenoids", *J. Appl. Phys.*, 48(5) (2001) 2000–2008.
[3] J. Jones, **"Contact Mechanics"**, Cambridge University Press (Cambridge, UK) (2000), Ch.6, p.56.
[4] Y. Lee, S.A. Korpela and R. Horne, "Structure of Multi-Cellular Natural Convection in a Tall Vertical Annulus", Proceedings of 7th International Heat Transfer Conference, U. Grigul et al., eds., Hemisphere (Washington DC), 2 (1982) 221–226.
[5] M. Hashish, "Waterjet Technology Development", High Pressure Technology, PVP-Vol. 406 (2000) 135-140.
[6] D.W. Watson, "Thermodynamic Analysis", ASME Paper No. 97-GT-288 (1997).
[7] C.Y. Tung, "Evaporative Heat Transfer in the Contact Line of a Mixture", Ph.D. thesis, Rensselaer Polytechnic Institute, Troy, NY (1982).

PROOFS

Authors will receive proofs of papers and are requested to return one corrected copy as a WORD file on a compact disc (CD) or by email. New materials inserted in the original text without Editor's permission may cause rejection of paper.

COPYRIGHT FORM

Author(s) will be asked to sign the IJAP Copyright Form and hence transfer copyrights of the article to the Journal soon after acceptance of it. This will ensure the widest possible dissemination of information.

OFFPRINTS

Authors will receive electronic offprint free of charge and any additional reprints can be ordered.

SUBSCRIPTION AND ORDERS

Annual fees (4 issues per year) of subscription are:
50 US$ for individuals inside Iraq; **200** US$ for institutions inside Iraq;
100 US$ for individuals abroad; **300** US$ for institutions abroad.
Fees are reduced by 25% for I.S.A.R.E.S.T. members. Orders of issues can be submitted by contacting the editor-in-chief or editorial office at admin@iraqiphysicsjournal.com, or editor_ijap@yahoo.co.uk to maintain the address of issue delivery and payment way.

IRAQI JOURNAL OF APPLIED PHYSICS
Vol. 18, No. 3, July-September 2022, pp. 3-10

Fabrication and Characterization of Silver-Doped Nickel Oxide Thin Films for Gas Sensors

Qayes A. Abbas[1]
Mohammed A. Hameed[2]
Ahmed S. Ahmed[2]

[1] *Department of Physics, College of Science, University of Anbar, Ramadi, IRAQ*
[2] *Department of Physics, College of Science, University of Baghdad, Baghdad, IRAQ*

The work includes fabrication of undoped and silver-doped nanostructured nickel oxide in form thin films, which use for applications such as gas sensors. Pulsed-laser deposition (PLD) technique was used to fabricate the films on a glass substrate. The structure of films is studied by using techniques of x-ray diffraction, SEM, and EDX. Thermal annealing was performed on these films at 450°C to introduce its effect on the characteristics of these films. The films were doped with a silver element at different doping levels and both electrical and gas sensing characteristics were studied and compared to those of the undoped films. Reasonable enhancements in these characteristics were observed and attributed to the effects of thermal annealing as well as doping with silver. Gas sensing measurements were carried out using NO_2 as a gaseous species to be detected. The results showed that the electrical conductivity, density as well as mobility of charge carriers, and gas sensitivity were affected by the doping level and annealing treatment.

Keywords: Gas sensor; Nickel oxide; Nanostructures; Pulsed-laser deposition
Received: 23 March 2022; **Revised:** 13 May 2022; **Accepted:** 20 May 2022

1. Introduction

Nanomaterial oxide such as a nickel oxide (NiO) is one of the transition metal oxides that has been extensively studied in recent decades. It has physical and chemical interested properties like NaCl-like structure and antiferromagnetic oxides. As well, it has given favorable candidate for plentiful industrial applications like thermal absorber [1], photo-electrolysis [2], catalyst for oxygen evolution [3], and electrochromic equipment [4,5]. Also, NiO was well-prepared matter used in the electrodes of batteries [6,7]. The pure crystals of NiO are idealistic insulators [8,9] and many research fields have explained and resolved the insulation property of NiO [10,11]. Perceivable conductivity is done in NiO via producing Ni vacancies or substituted atoms of some alkali metals (e.g. Li) for Ni sites to fabricate rechargeable batteries [6,12]. During the last two decades, many works on doping NiO thin films with silver in atomic form have shown that such devices are highly efficient to detect very small amounts of several gaseous species as well as sunlight and electromagnetic radiation [13-16]. This multipurpose performance is not common for all similar structures.

Gas sensing applications are drastically increasing due to their industrial, environmental, and clinical importance. Meanwhile, fabrication of efficient sensors for as many as possible types of gases is the main goal of too much research works especially for gases having dangerous or harmful effects on all types of lives on the earth [17-21]. Coinciding with the revolution of nanotechnology and advanced materials, reasonable enhancements in the performance of gas sensing devices were achieved [22,23]. Amongst, metal oxide nanostructures doped with appropriate elements are dominating the industrial and environmental applications of gas sensors. Such devices can be fabricated by flexible techniques such as pulsed-laser deposition (PLD) [4,24].

The aim of this work is to study undoped and silver-doped nanostructured NiO thin films fabricated using PLD method. Both electrical and gas sensing characteristics of these structures were compared.

2. Experimental Part

The main parts of PLD technique are schematically illustrated in Fig. (1). This technique is used to prepare NiO, where the test chamber is first evacuated down to 0.001 mbar. A focused beam of Q-switched Nd:YAG laser working in the second harmonic generation (SHG) is entered the chamber through a window and directed at 45° on the surface of NiO target. The target was made as a disc from NiO nanopowder pressed as 5cm in diameter and ~2mm in thickness. One side of this disc was polished to be mirror-like. The surface of glass substrate and target surface was parallel to each other. The appropriate gap was preserved between the substrate and the used target, this makes the incident laser beam avoiding any hamper by the substrate holder. For doping experiment, silver nanopowder was mixed at different weight percentage amounts with the NiO nanopowder. The mixture was then compressed, cut and polished to form the Ag-doped NiO target. Some experimental parameters such as rotating the NiO

disc, the substrate annealing temperature and placement the target with respect to the substrate, were easily possible during the work. The structure of the prepared films was investigated using a Shimadzu 6000 X-Ray Diffractometer with Cu(kα) radiation source of 1.5406Å wavelength. The range of scanning angle (2θ) has been varied from 20 to 70 degrees and a speed of 4 deg/min. The scanning electron microscopy (SEM) and energy-dispersive x-ray spectroscopy (EDX) have been used with 15 and 10 kx magnifications.

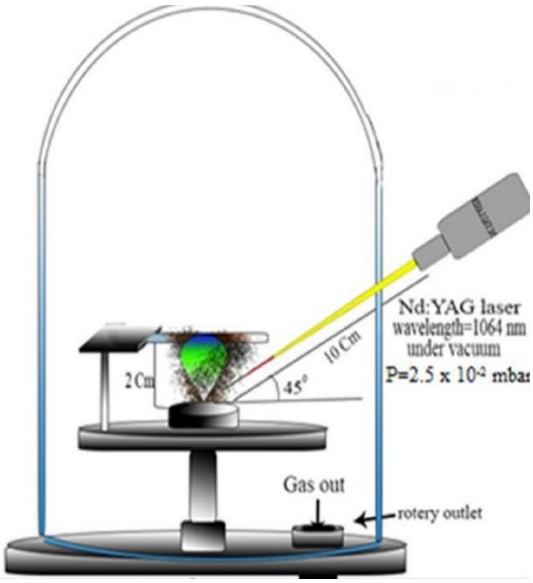

Fig. (1) Schematic diagram of main parts of PLD system [22]

Nickel oxide (NiO) powder with 99.99% purity and silver (Ag) powder with 99.9% purity were used to prepare thin films. The targets of bulk $NiO_{(1-x)}$:Ag_x have been prepared from both materials by grinding and mixing them at various concentrations (x= 0, 0.1, 0.2, 0.3 or 0.4 at.%) for 10 minutes, then pressed into pellets with 1.2 cm diameter using a SPECAC hydraulic press to apply a pressure of 6 tons/cm^2 for 10 minutes. The prepared targets of the pure NiO and Ag-doped NiO were used to prepare thin films using PLD method. Both undoped and doped samples were annealed at 450 °C using electrical furnace at atmospheric pressure for two hours for recrystallization. Thickness of the prepared films was measured using optical interferometer method. To affirm the electrical conductivity, the type of conductivity, and gas sensing measurements, interdigitated aluminum Ohmic metal contacts were deposited on the Ag:NiO films by using vacuum evaporation technique. Four-point probe (F.P.P.) method was processed on 1x1-cm^2 sheets, and for electrical properties 1mm interdigitated distance.

The experimental gas sensor system involves a test chamber of stainless steel cylinder of 15cm in diameter and 15cm in length of 15cm. This chamber contains an inlet to inflow the gas to be tested and an entry valve to inflow the atmosphere after emptying. The electrical conducting points are connected to the heater by multi-pin feedthrough at the body of the chamber. Also, sensing electrodes and thermocouples of K-type have been used. Inside this chamber, the sensor part is located upon the heater. A conductive aluminum sheet is used to connect the electrical connections of the multimeter pins with the sensor sample.

To clean the chamber from contamination, a rotary pump is used to evacuate it down to about 1 mbar. A temperature controller is used to set the gas sensor at the required temperature. Finally, to measure the change in resistance, a PC-interfaced digital multimeter is used. These processes are repeated for all operation temperatures.

3. Results and Discussion

Figure (2) represents the XRD pattern of the sample annealed at 450°C for two hours. It showed that the planes (111), (200), and (220) correspond to angles of 32.9°, 43.7°, and 63.0° respectively, which are matched with the JCPDS file 73-1523 [25]. Also, it is found that the prepared structure is quadrilateral and polycrystalline.

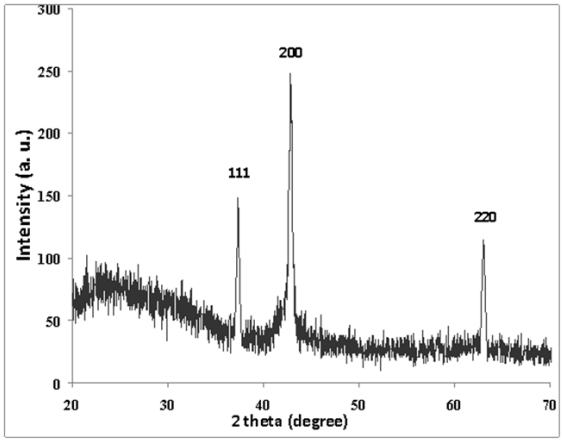

Fig. (2) XRD pattern of 3% Ag:NiO sample annealed at 450°C for two hours

Figure (3) shows SEM images and EDX result for 3% Ag-doped NiO thin film. The SEM images are shown that the particles have several morphologies. They have different tiny asymmetrical nano-size clusters. Furthermore, the sample has various grain sizes ranging from 50 to 500 nm. The EDX is carried out to determine the elemental composition of the film sample. It emphasizes in a qualitative mode the presence of oxygen (O), silicon (Si), nickel (Ni), and silver (Ag) atoms that compose the sample.

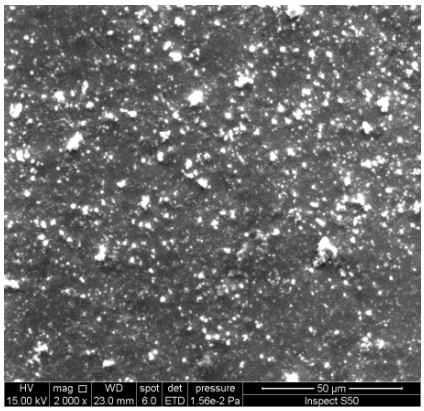

(a)

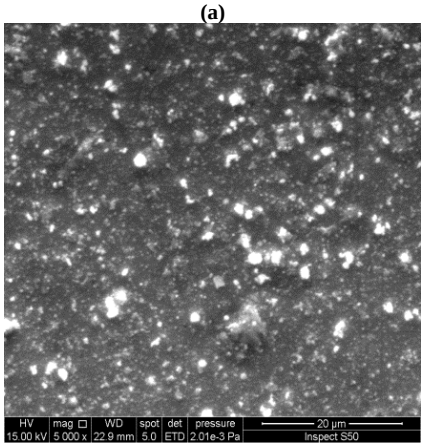

(b)

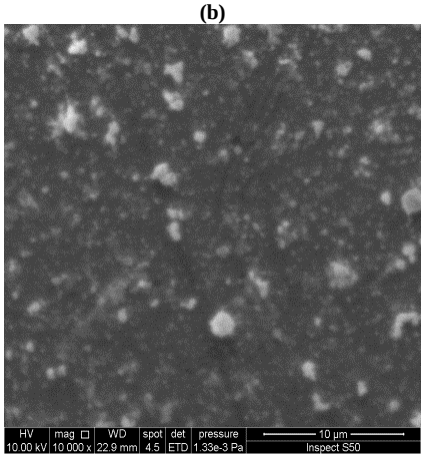

(c)

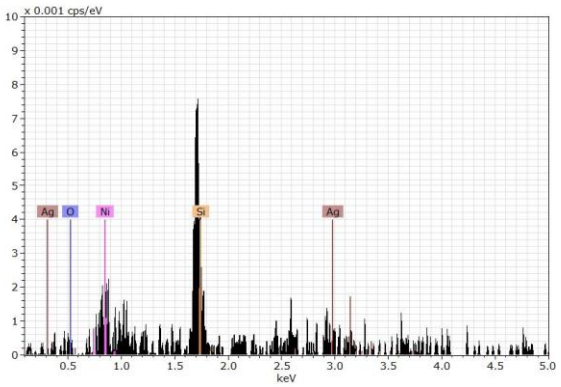

Fig. (3) SEM and EDX results for 3% Ag-doped NiO thin film prepared by PLD technique. SEM result is presented in three magnification scales (50, 20 and 10 µm)

Figure (4) exhibits the variation of the electrical conductivity (Lnσ) with the reciprocal temperature (1000/T) of as-prepared and annealed NiO thin films of both types (undoped and Ag-doped). Thermal annealing was performed at 450°C in order to induce the structural distribution of NiO grains over the prepared thin films. This thermal annealing may have another effect to enhance the substitutional doping of NiO structure with Ag atoms. Both effects were compared to the as-prepared undoped NiO samples. It is clear that increasing temperature causes the electrical conductivity to increase as the charge carriers are provided with higher kinetic energy to move and generate electrical signal with higher intensity. Similarly, higher level of doping with silver causes the electrical conductivity to increase as more silver atoms contribute to the electrical conduction of the doped NiO sample. Doping level of 4% has increased the electrical conductivity of both as-prepared and annealed samples by 150% when compared to the undoped sample.

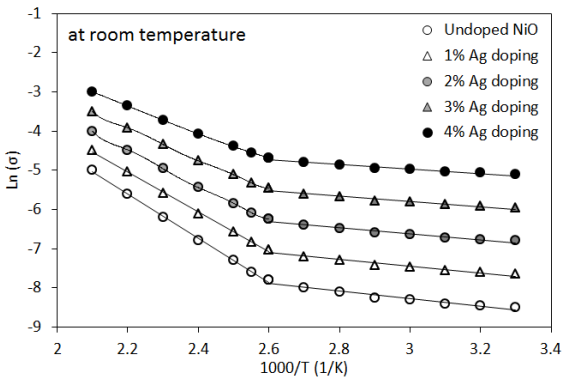

(a)

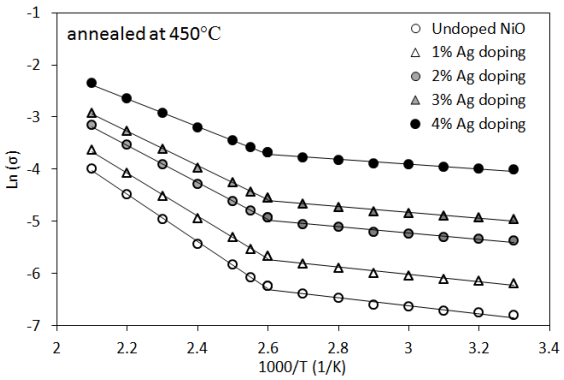

(b)

Fig. (4) Variation of Ln(σ) with 1000/T for undoped and Ag-doped NiO samples (a) as-prepared (at room temperature) and (b) annealed at 450°C

Variety of mechanisms can be used to explain the electrically conductive behavior of polycrystalline NiO thin films. Extrinsic impurities are giving the ability to grow in impurity conduction behavior at depressed temperatures and band conduction close to and higher than the room temperature. The grain boundary works as shipping traps, controlling the potential barriers and barriers throughout the grain, which makes the electric conductivity of these films

influenced [26,27]. Additionally, when the semiconductor is at low temperatures, or heavily doped, the dominated current of band conduction is caused by emitted thermal-field of the carriers through the barrier, and at high temperatures or in lightly doped material, thermionic emission dominates over the barrier [28-30]. These processes are taken into account in the analysis of the electrical transport properties of prepared samples in the present study.

The Hall measurements showed that pure and Ag-doped NiO thin film samples are p-type semiconductors. For p-type samples, the Hall parameters involve the electrical conductivity (σ), Hall effect coefficient (R_H), carrier concentration (n_H), and mobility (μ_H).

At room temperature, the electrical conductivity (σ_{RT}) of the annealed samples was determined and compared to that of as-prepared samples, as shown in Fig. (5). The effects of silver doping ratio as well as thermal annealing are very clear, as the electrical conductivity was increased by 36.4% at silver doping ratio of 4% compared to the as-prepared sample doped at the same ratio, while an increase of 23.8% was determined at doping ratio of 1% compared to the as-prepared sample doped at the same level. So, increasing the Ag doping level by 400% has resulted in a consequent increase in the electrical conductivity of about 13%. As the doping ratio is increased, additional dopant atoms occupy sites of Ni atoms in NiO lattice and result in increasing charge carriers. The essential objective of doping NiO crystalline structure with silver is to produce more charge carriers and thus increasing the electrical signal during the response to the tested gas.

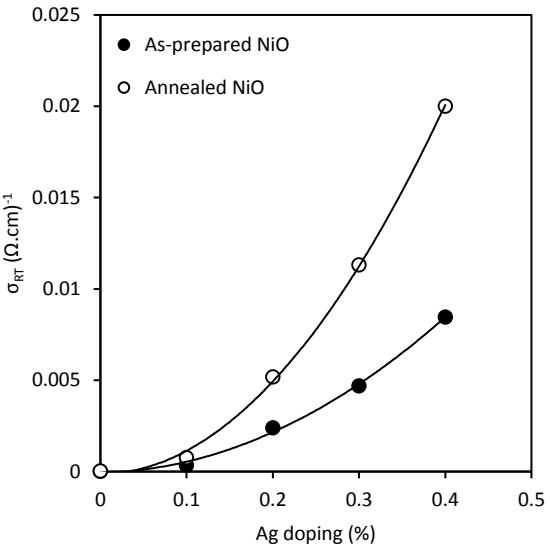

Fig. (5) Variation of room-temperature electrical conductivity (σ_{RT}) with Ag doping level (%) for as-prepared and annealed (at 450°C) NiO thin films

The variation in the density of charge carriers with doping level was determined as shown in Fig. (6). It was observed that the average increase in the density of charge carriers of Ag-doped NiO samples due to thermal annealing was about 79% when compared to the as-prepared Ag-doped NiO samples. Thermal annealing allows Ag atoms to substitute Ni atoms in the NiO structure much more effectively and thus additional charge carriers are provided and the electrical conduction is increased. However, thermal annealing has resulted in an increase of 200% leading to arise in the density of charge carriers for the undoped NiO films.

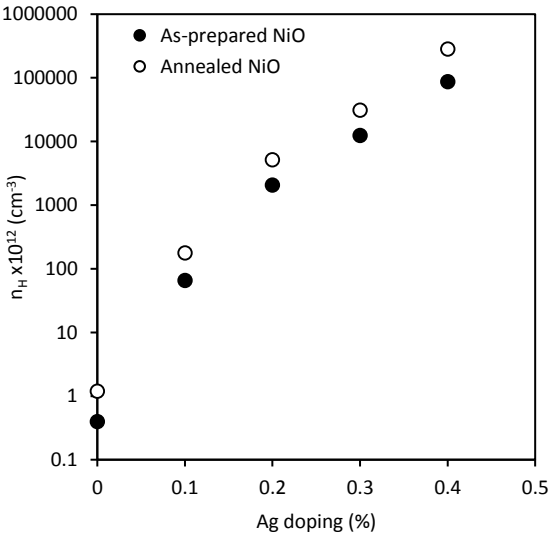

Fig. (6) Variation of carrier concentration (n_H) as a function of Ag doping level (%) for as-prepared and annealed (at 450°C) NiO thin films

Figure (7) shows the variation of mobility (μ_H) with percentage doping level for both as-prepared and annealed samples. The thermal annealing of the pure NiO sample affects the mobility of the charge carriers by increasing it by 145%. In existence of Ag dopants, the mobility was slightly decreased. High dopant concentration leads to the ionized impurity scattering from the substitutional donors and scattering from the interstitials [31,32], resulting in a decrease in the mobility.

The aggregate variation that occurs in the mobility and density of charge carriers can be demonstrated as the position of Ag dopants in the NiO structure. The mobility of charge carriers was reduced at the higher doping concentrations which could be resulted from the interstitial occupancy of Ag atoms in NiO structure. The appearance of Ag dopants at interstitial sites and grain boundaries in oxide form, and diminishing grain size, may act as scattering centers and lead to a remarkable decrease in the mobility at a high dopant concentration. From this result, one may conclude that low doping level of NiO with Ag atoms improves the conductivity of the film as the electrical conductivity of Ag element is higher than that of NiO.

The prepared samples have been tested as sensors to detect the harmful NO_2 gas at different operation temperatures. The sensitivity (S) is determined by the following equation [33]:

$$S = \left|\frac{R_g - R_a}{R_a}\right| \times 100\% \quad (1)$$

where R_a and R_g are the electric resistances of the samples in air and in existence of tested gas, respectively

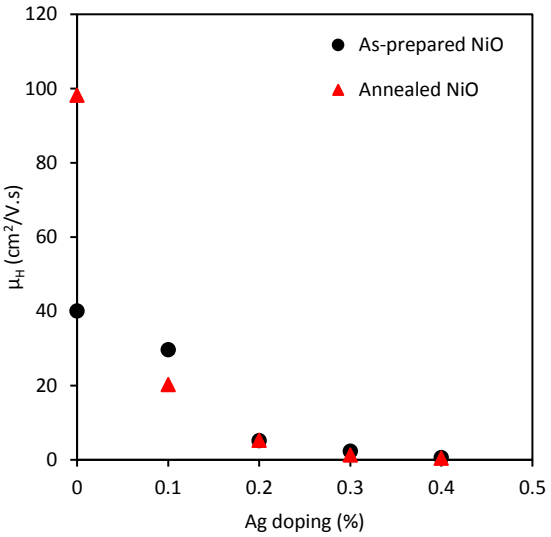

Fig. (7) Variation of mobility (μ_H) with Ag doping level (%) for as-prepared and annealed (at 450°C) NiO thin films

Figure (8) illustrates the variation of resistance of Ag-doped NiO thin films to NO_2 gas at operation temperature for different measurement times (30, 60 and 90 min). The resistance has been increased as the operation temperature reaches to 200°C for measuring times of 30 and 60 min, while the maximum resistance was reached at 260°C for measuring time of 90 min. The two behaviors were identical, which means that the Ag-doped NiO samples as gas sensors work preferably at elevated temperatures in comparison with those at lower temperatures (<200°C). However, further increase in operation temperature led to decrease the sensitivity of these devices.

In order to introduce the effect of doping with silver on the performance of the fabricated gas sensors, the resistance of undoped and Ag-doped NiO samples has been tested with time. From this figure, the mechanism of a variable resistance depends on the time before exposing the NiO samples to NO_2 gas. The system was left to stabilize at its operation temperature for about 15 min, thus the stabilized resistance is assigned as R_a (Gas_{on}). During exposing the sample to the NO_2 gas, the resistance is reduced and assigned as R_g (Gas_{off}). The species of NO_2 gas react with oxygen ions on the surface of the sample and therefore, the oxidation mechanism leads to rising the quantity of the free carriers. Thus, the resistance of the samples reduces when exposed to oxidant gases.

The sensitivity was measured at higher operation temperatures as presented in Fig. (9). The sensitivity of prepared films is growing with increasing operation temperature to 200°C. The vibration of NiO molecules and the speed of gas diffusion are increased as a result of increasing the temperature and this results in gas adsorption. The desorption rate of the sample's surface raises and thus the sensitivity is increased according to the increase in the temperature. The higher sensitivity of Ag-doped NiO samples achieved in this work was about ~79% at an operation temperature of 200°C.

Furthermore, the required parameters to design the gas sensing devices include the response time, which is the time required for the sensor to realize 90% of the maximum variation in resistance in the presence of the detected gas. Another considerable parameter is the recovery time, which can be denoted as the time required to go back to 10% of the higher resistance of the sensor device. These two parameters were tested at a bias voltage of 6 V. All results in table (1) for both parameters are decreased according to increasing the operation temperature when sensing NO_2 gas.

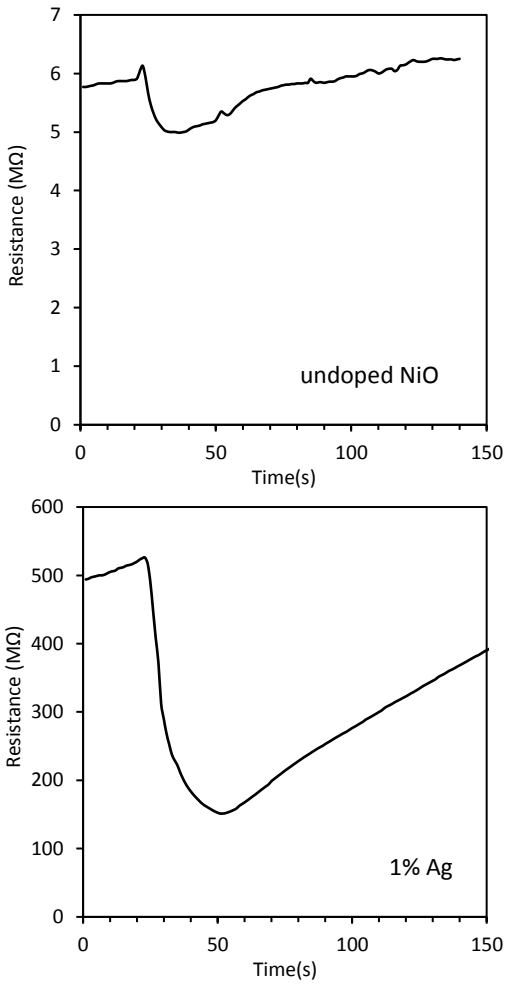

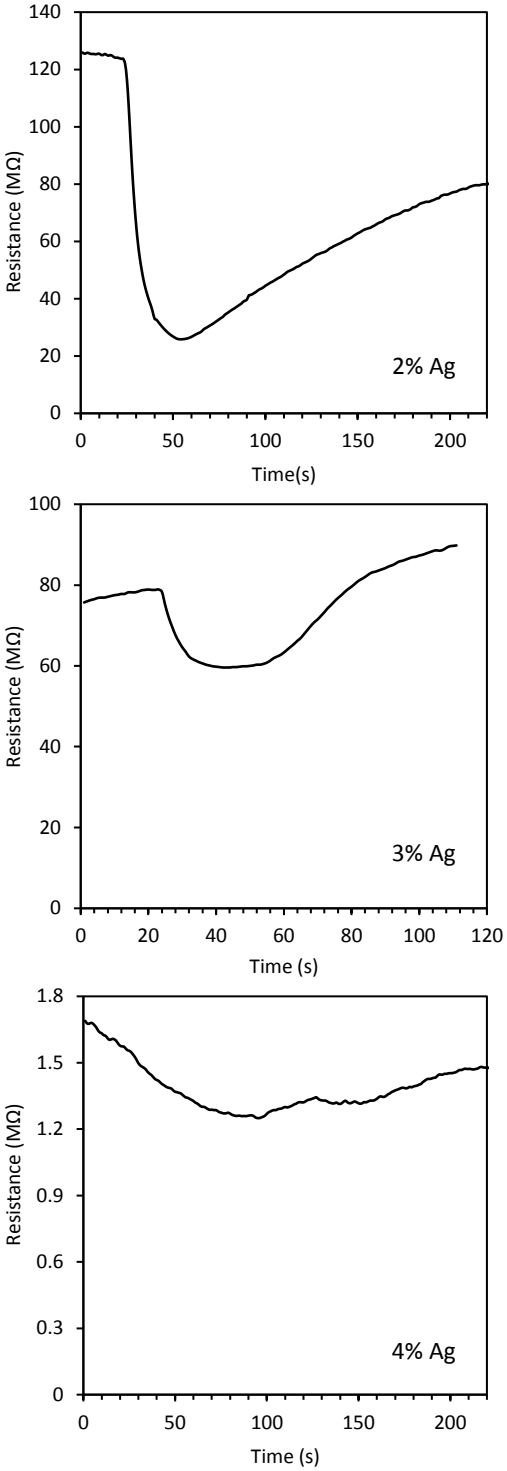

Fig. (8) Variation of thin film sample resistance (R) with time for annealed (at 450°C) undoped and Ag-doped NiO thin films at operation temperature of 200°C

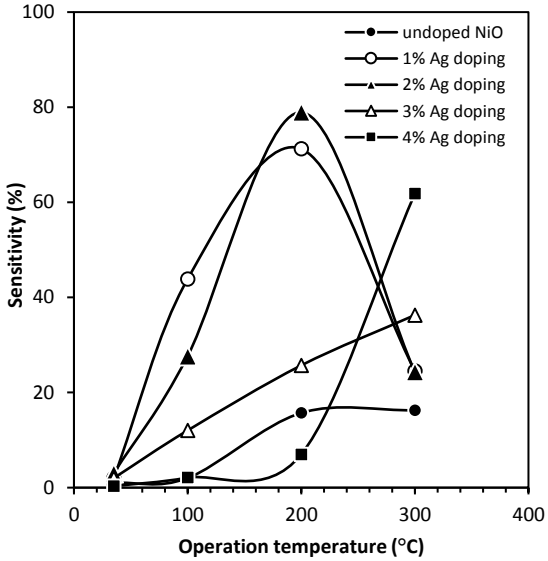

Fig. (9) Variation of sensitivity of Ag-doped NiO thin films to NO_2 gas with operation temperature for different measurement times

Table (1) Results of response time and recovery time of Ag-doped NiO thin film gas sensors at different operation temperatures

T (°C)	Undoped NiO		1% Ag doping		2% Ag doping	
	Response time (s)	Recovery time (s)	Response time (s)	Recovery time (s)	Response time (s)	Recovery time (s)
35	-	-	-	-	-	-
100	25.2	221.4	31.5	216.9	42.3	117.9
200	26.1	133.2	25.2	134.1	14.4	56.7
300	19.8	49.5	19.8	58.5	36	76.5

T (°C)	3% Ag doping		4% Ag doping	
	Response time (s)	Recovery time (s)	Response time (s)	Recovery time (s)
35	32.4	216	-	-
100	29.7	126.9	24.3	89.1
200	35.1	97.2	25.2	61.2
300	27.9	84.6	9.9	60.3

4. Conclusion

In concluding remarks, pulsed-laser deposition was used to prepare Ag-doped NiO thin films. These films were thermally annealed at 450°C and their electrical characteristics were affected by the Ag doping levels. Doping level of 4% has increased the electrical conductivity of both as-prepared and annealed samples by 150%. The average increase in the density and mobility of charge carriers of Ag-doped NiO samples due to thermal annealing were about 79% and 145%, respectively. The overall variation in the density and mobility of charge carriers can be interpreted according to the position of Ag atoms within the NiO crystalline structure. The Ag-doped NiO thin film gas sensors operate better at

elevated temperatures when compared to the lower temperatures (<200°C). The maximum gas sensitivity of Ag-doped NiO samples was ~79% at operation temperature of 200°C.

Acknowledgment

Authors would like to acknowledge the University of Baghdad and the University of Anbar for their support to this work.

References

[1] J. Huang and Q. Wan, "Gas Sensors Based on Semiconducting Metal Oxide One-Dimensional Nanostructures", Sensors, 9 (2009) 9903-9924.

[2] O.A. Hamadi, N.J. Shakir and F.H. Hussain, "Magnetic Field and Temperature Dependent Measurements of Hall Coefficient in Thermal Evaporated Tin-Doped Cadmium Oxide Thin Films", Bulg. J. Phys., 37(4) (2010) 223-231.

[3] M.D. Irwin et al., "Structural and electrical functionality of NiO interfacial films in bulk heterojunction organic solar cells", Chem. Mater., 23 (2011) 2218-2226.

[4] P. Mallick and N.C. Mishra, "Evolution of structure, microstructure, electrical and magnetic properties of nickel oxide (NiO) with transition metal ion doping", Am. J. Mater. Sci., 2(3) (2012) 66-71.

[5] B.S. Kwak et al., "Synthesis of spherical NiO nanoparticles using a solvothermal treatment with acetone solvent", J. Indust. Eng. Chem., 18 (2012) 11-15.

[6] A.M. Soleimanpour, A.H. Jayatissa and G. Sumanasekera, "Surface and gas sensing properties of nanocrystalline nickel oxide thin films", Appl. Surf. Sci., 276 (2013) 291-297.

[7] G. Zhang et al., "Synthesis of one-dimensional hierarchical NiO hollow nanostructures with enhanced supercapacitive performance", Nanoscale, 5 (2013) 877-881.

[8] M. Barman, S. Paul and A. Sarkar, "Electronic properties in Mn doped and pure NiO clusters", Proc. Int. Conf. on Recent Trends in Appl. Phys. Mater. Sci. (RAM 2013), Bikaner, Rajasthan, India, 1-2, (2013) 427-428.

[9] Y.A. Kumar Reddy, A. Sivasankar Reddy and P. Sreedhara Reddy, "Influence of oxygen partial pressure on the physical properties of Ag doped NiO thin films", Proc. Int. Conf. on Recent Trends in Appl. Phys. Mater. Sci. (RAM 2013), Bikaner, Rajasthan, India, 1-2, (2013) 475-476.

[10] S.H. Faisal and M.A. Hameed, "Heterojunction Solar Cell Based on Highly-Pure Nanopowders Prepared by DC Reactive Magnetron Sputtering", Iraqi J. Appl. Phys., 16(3) (2020) 27-32.

[11] R.H. Turki and M.A. Hameed, "Spectral and Electrical Characteristics of Nanostructured NiO/TiO_2 Heterojunction Fabricated by DC Reactive Magnetron Sputtering", Iraqi J. Appl. Phys., 16(3) (2020) 39-42.

[12] J.W. Jung, C.-C. Chueh and A.K.-Y. Jen, "A Low-Temperature, Solution-Processable, Cu-Doped Nickel Oxide Hole-Transporting Layer via the Combustion Method for High-Performance Thin-Film Perovskite Solar Cells", Adv. Mater., 27(47) (2015) 7874-7880.

[13] X. Wang and Z. Wei, "Optical Properties of Silver Doped NiO Films Prepared by Spray Pyrolysis Method", J. Adv. Microsc. Res., 10(1) (2015) 24-27(4).

[14] A.V. Kadu, S.V. Jagtap and N.N. Gedam, "Preparation and Gas Sensing Performance of Nanostructured Copper Doped Nickel Oxides", Int. J. Chem. Phys. Sci., 4 (2015) 186-194.

[15] O.A. Hammadi, M.K. Khalaf and F.J. Kadhim, "Fabrication of UV Photodetector from Nickel Oxide Nanoparticles Deposited on Silicon Substrate by Closed-Field Unbalanced Dual Magnetron Sputtering Techniques", Opt. Quantum Electron., 47(12) (2015) 3805-3813.

[16] M.A. Hameed, S.H. Faisal and R.H. Turki, "Characterization of Multilayer Highly-Pure Metal Oxide Structures Prepared by DC Reactive Magnetron Sputtering Technique", Iraqi J. Appl. Phys., 16(4) (2020) 25-30

[17] J.A. Dirksen, K. Duval and T.A. Ring, "NiO thin-film formaldehyde gas sensor", Sen. Actuat. B: Chem., 80(2) (2001) 106-115.

[18] I. Hotovy et al., "Sensing characteristics of NiO thin films as NO_2 gas sensor", Thin Solid Films, 418 (1) (2002) 9-15.

[19] X.H. Xia et al., "Electrochromic properties of porous NiO thin films prepared by a chemical bath deposition", Solar Energy Mater. Solar Cells, 92 (2008) 628-633.

[20] B. Varghese et al., "Fabrication of NiO nanowall electrodes for high performance lithium ion battery", Chem. Mater., 20 (2008) 3360-3367.

[21] M. Stamataki et al., "Hydrogen gas sensors based on PLD grown NiO thin film structures", phys. Stat. sol. a, 205(8) (2008) 2064-2068.

[22] I. Simon et al., "Selected gas response measurements using reduced graphene oxide decorated with nickel nanoparticles", Nano Mater. Sci., 3 (2021) 412-419

[23] B. Sowmya, J. Athira and P.K. Panda, "A review on metal-oxide based p-n and n-n heterostructured nano-materials for gas sensing applications", Sens. Int., 2 (2021) 100085.

[24] O.A. Hamadi, "Characteristics of CdO-Si Heterostructure Produced by Plasma-Induced Bonding Technique", Proc. IMechE, Part L, J. Mater.: Design & Appl., 222 (2008) 65-71.

[25] H.E. Swanson et al., **"Standard X-ray Diffraction Powder Patterns"**, US Dept. Commerce, NBS sec. 1 (1962) 47.

[26] O. Kingsley et al., "Efficient p-type doping of sputter-deposited NiO thin films with Li, Ag, and Cu acceptors", Phys. Rev. Mater., 4 (2020)

104603.
[27] Y. Wei et al., "Improving the efficiency and environmental stability of inverted planar perovskite solar cells via silver-doped nickel oxide hole-transporting layer", Appl. Surf. Sci., 427(B) (2018) 782-79.
[28] A.S. Ahmed and M.A. Hameed, "Widening of the optical band gap of $CdO_{2(1-X)}Al_{(X)}$ thin films prepared by pulsed laser deposition", Appl. Phys. A, 127 (2021) 188.
[29] M.T. Ramesan and V. Santhi, "Synthesis, characterization, conductivity and sensor application study of polypyrrole/silver doped nickel oxide nanocomposites", Composite Interfaces, 25 (8) (2018) 725-741.
[30] X. Xia et al., "Lithium and Silver Co-Doped Nickel Oxide Hole-Transporting Layer Boosting the Efficiency and Stability of Inverted Planar Perovskite Solar Cells", ACS Appl. Mater. Interfaces, 10(51) (2018) 44501-44510.
[31] J. Zheng et al., "Solution-Processed, Silver-Doped NiOx as Hole Transporting Layer for High-Efficiency Inverted Perovskite Solar Cells", ACS Appl. Energy Mater., 1(2) (2018) 561-570.
[32] O.A. Hammadi and N.E. Naji, "Fabrication and Characterization of Polycrystalline Nickel Cobaltite Nanostructures Prepared by Plasma Sputtering as Gas Sensor", Phot. Sen., 8(1) (2018) 43-47.
[33] I.M. Ali et al. "Structural, Optical and Sensing Behavior of Neodymium-Doped Vanadium Pentoxide Thin Films", Iranian J. Sci. Technol. Trans. Sci., 42 (2018) 2375-2386.

IRAQI JOURNAL OF APPLIED PHYSICS
Vol. 18, No. 3, July-September 2022, pp. 11-17

Characteristics of Multilayer glass/ITO/N:TiO_2/NiO/KOH/Pt/glass Photoelectrochromic Device Synthesized by Reactive Magnetron Sputtering

Manal A. Aziz
Firas J. Jawad

Department of Physics, College of Science, University of Baghdad, Baghdad, IRAQ

In this work, titanium dioxide doped with nitrogen (N-doped TiO_2), as electrochromic layer (EC), and nickel oxide (NiO), as ion storage layer (IS), have been synthesized by dc reactive magnetron sputtering technique. The synthesized layers have been characterized using x-ray diffraction (XRD), field-emission scanning electron microscopy (FE-SEM), Fourier-transform infrared (FTIR) and UV-visible spectroscopy. Mixed-phase (anatase/rutile) has been observed for EC layer (TiO_2) and cubic phase structure for IS layer (NiO). The nanostructures of these layers, on both silica and indium tin oxide (ITO) substrates, have been investigated and determined. The photoelectrochromic device with the configuration of glass/ITO/N:TiO_2/NiO/KOH/Pt/glass has been fabricated and characterized. The multilayers configuration of this photoelectrochromic device has been tested by applying ±3.4V voltages with xenon-light irradiation and high optical transmittance of about 23% has been determined.

Keywords: Photoelectrochromic; Smart window; Metal oxides; Magnetron sputtering
Received: 07 April 2022; **Revised:** 18 May 2022; **Accepted:** 25 May 2022

1. Introduction

Smart windows can control the amount of visible light and solar radiation that enters a structure, as well as provide energy efficiency by varying the transmittance levels based on dynamic needs [1-3]. Electrochromic materials are materials capable of changing their optical properties when ions are intercalated or DE intercalated as an electric field is applied. Because of this property, these materials can be used to create electrochromic devices that control properties like transmittance and absorbance [4-9].

Titanium dioxide (TiO_2) is a semiconductor having good chemical stability, a high refractive index, and low nontoxicity [10]. A robust TiO_2 is an effective material for applications such as gas sensors [11], dielectrics in semiconducting field-effect transistors [12], and photoelectrochromic (PEC) devices [13]. Doping TiO_2 with non-metallic elements such as nitrogen has received special attention [14-18]. The use of these anionic dopants causes bandgap narrowing, and effectively extends TiO_2 absorption threshold into the visible range [19]. Nickel oxide (NiO) is a semiconducting compound crystallizing in either cubic or hexagonal structure. This material exhibits properties of a p-type semiconductor with a band gap ranging from 3.4 to 4.0 eV [20]. Due to its low cost, strong cycle reversibility, and good coloration efficiency, nickel oxide exhibits electrochromic qualities that make it a promising option as an anodic material in electrochromic devices (ECD) [21].

There are many techniques used to prepare the electrochromic layer such as chemical vapor deposition (CVD), sol-gel, and sputtering. The sputtering as a deposition technique is one of the most widely used techniques to prepare thin films. To improve the deposition rate using the basic sputtering process was developed. Deposition at room temperature is one of the most important advantages of the sputtering deposition process [22].

In the presented work, multilayers were prepared using dc reactive magnetron sputtering technique and their structural and optical characteristics were optimized in order to fabricate multilayers glass/ITO/N:TiO_2/NiO/KOH/Pt/glass configuration as photoelectrochromic (PEC) device.

2. Experimental Work

2.1 Materials

Highly-pure titanium sheet with 80 mm diameter and 0.5 mm thickness and highly-pure nickel sheet with 80 mm diameter and 0.3 mm thickness were used. Indium tin oxide (ITO) glass substrates with 100 mm diameter and 0.7 mm thickness supplied by Guangdong (China) and potassium hydroxide (KOH) supplied by CDH (India) were used too.

2.2 Preparation of Multilayers and PEC device

Nitrogen-doped titanium dioxide (N:TiO_2) was deposited as the electrochromic (EC) layer using a homemade dc reactive magnetron sputtering technique. The titanium sheet was maintained on the cathode. A voltage of 2000 V and current of 40 mA

were applied between the electrodes. Thin films of N-doped TiO_2 were prepared with different ratios of the gas mixtures $Ar:O_2:N_2$. The ratios of gases in the mixture were varied as 76:19:5, 43:42:15, 40:40:20, and 30:60:10. The deposition time was fixed at two hours for all samples. There was no intentional heating of the substrates in this work.

Nickel oxide (NiO) was deposited as an ion storage (IS) layer using the same sputtering technique. The nickel sheet was placed on the cathode. A voltage of 2500 V and current of 50 mA were applied between the electrodes. An $Ar:O_2$ gas mixture of 50:50 was used. The deposition time was set to 2, 3, and 4 hours.

Two transition metal oxide thin films ($N:TiO_2$ and NiO) were deposited on transparent conductive layers of ITO to configure multilayers $ITO/N:TiO_2/NiO$ PEC device as shown in Fig. (1a).

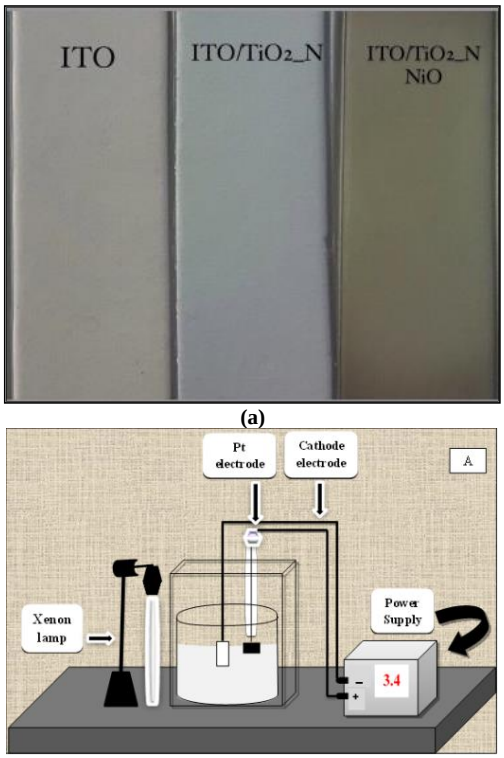

Fig. (1) (a) Layer configurations and (b) schematic diagram of the system smart window

The multilayers electrode was dipped as the cathode and the platinum electrode as the anode in an electrolyte solution of 1M KOH. The electrodes were connected to a power supply of 3.4 V under xenon-light irradiation within 2 minutes to obtain the colored state. In the bleached case, the electrodes were reversed, the voltage of 4 eV was increased, and the time also increased to approximately 3 minutes. Both the colored and bleached states were obtained through oxidation and reduction processes for the fabrication of the PEC device (smart window). Figure (1b) illustrates the schematic diagram of the system PEC device.

3. Results and Discussion

Figure (2a) shows the XRD pattern of the thin N-doped TiO_2 (mixed phase) prepared using $Ar:O_2:N_2$ gas mixture of 76:19:5 at an inter-electrode distance of 4 cm and deposition time of two hours. From the figure, the results confirmed that there are distinct diffraction peaks for both anatase and rutile phases of TiO_2. The observed peaks in the XRD pattern correspond to the (101), (004), (200), (105), (211), (118), (116), (220), and (215) planes of the TiO_2 anatase phase, while the planes (101), (111), (210), and (211) are corresponding to the TiO_2 rutile phase. The obtained results are consistent with the JCPDS card no. 21-1276 [23]. The planes (111) and (220) refer to the structure of titanium nitride and agree with the JCPDS card no. 1420-38 [24]. The XRD pattern maintains very intense and fine peaks to indicate proper crystallization. When the two phases of TiO_2 are found in the same sample, the anatase phase mass ratio (m_A) can be estimated from Eq. (1) [25,26]:

$$m_A = \frac{1}{\left[1+1.26\frac{I_R}{I_A}\right]} \quad (1)$$

where I_R is the rutile phase intensity at the (110) level and I_A is the anatase phase intensity at the (101) level

The results show that the mass percentage of anatase and rutile phases in the sample was 55.4%, and 44.6%, respectively.

The crystallite size was calculated by Scherrer's formula as [27]:

$$Crystallite\ size = \frac{0.9\,\lambda}{\beta\ cos\theta} \quad (2)$$

where λ is the wavelength of x-ray (1.5406Å), θ is the diffraction angle, and β is the full-width at half maximum (FWHM) of the extreme peaks

According to the highest peak intensity (101) for the anatase phase, (210) for the rutile phase, the results showed that the crystallite size of the N-doped TiO_2 thin film sample was 15.56 nm for the anatase phase and 17.77 nm for the rutile phase.

Figure (2b) shows the XRD pattern of the NiO thin film sample prepared using $Ar:O_2$ gas mixing ratio of 50:50, inter-electrode distance of 4 cm, and deposition time of 3 hours. The peaks in the XRD patterns are corresponding to the (111), (200), (220), (311), and (222) planes of the cubic crystal structure (FCC) of NiO. No peak was observed for any other phases, indicating the high purity of the NiO sample. The results indicate a high agreement in the intensity of the characteristic peaks and diffraction angles with the standard spectrum (JCPDS card no. 04-0835) [28]. The crystallite size was calculated using Scherrer's formula (Eq. 2) with the highest peak intensity (200). The results showed that the crystallite size was 12.64 nm.

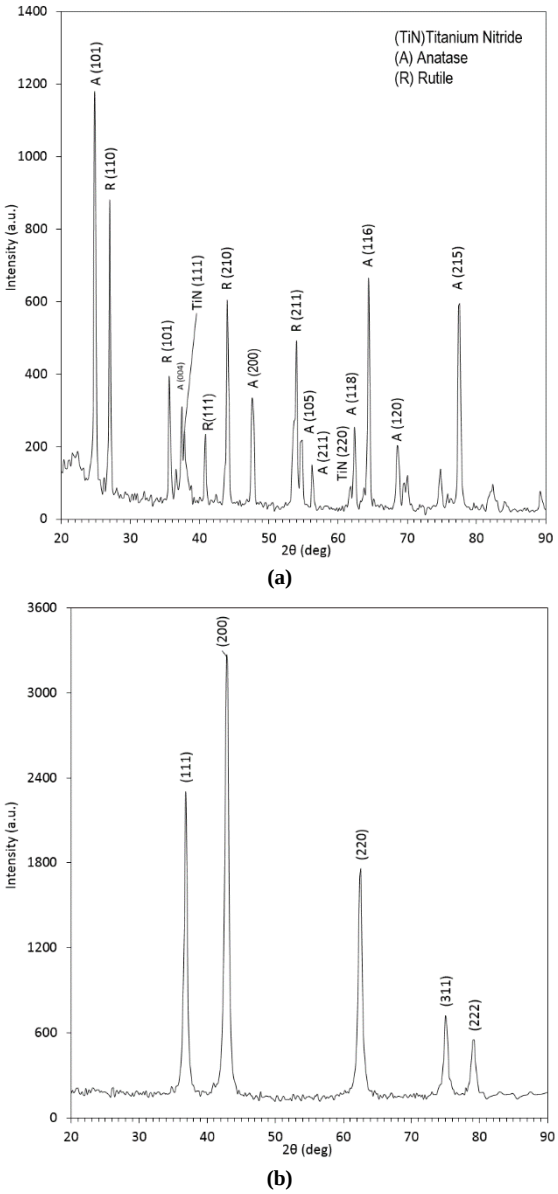

Fig. (2) XRD patterns of (a) N-doped TiO_2 thin film, and (b) NiO thin film

Figure (3) shows the FTIR spectra of the as-prepared N-doped TiO_2 and NiO thin films. The N-doped TiO_2 sample was prepared using a gas mixture of 76:19:5 and deposition time 2 hours, while the NiO sample was prepared using a gas mixture of 50:50 and deposition time 3 hours. The bands assigned to Ti-O symmetric and asymmetric stretching vibration modes were observed around 522 and 678 cm^{-1}, respectively, while the peak at 439 cm^{-1} is ascribed to Ti-O-Ti bonds in the TiO_2 lattice. The peaks around 3458 and 1643 cm^{-1} are attributed to the stretching and bending vibration of the OH group in water molecules in the atmosphere [29]. The bands around 1597, 1481 and 1348 cm^{-1} are attributed to the vibrations of the Ti–N bond [30], while the band at 885 cm^{-1} can be ascribed to the vibration of surface-absorbed N-O. The appearance of the N-Ti bond in the samples with varying N:TiO_2 ratios suggests that the N species have been incorporated into the TiO_2 lattice. Furthermore, the FTIR spectrum shows the absence of any impurities in the prepared samples and this is attributed to the optimization of operating conditions of the sputtering system, which is one of the most important advantages exhibited by this technique.

For NiO sample, the FTIR spectrum shows peaks at around 450.68 and 1294.77 cm^{-1} which are due to the Ni-O stretching vibrations [31]. The wideband centered at 3414.45 cm^{-1} is for O-H stretch vibration. The observed peak at 1574.66 cm^{-1} is assigned to the H-O-H bending vibration mode.

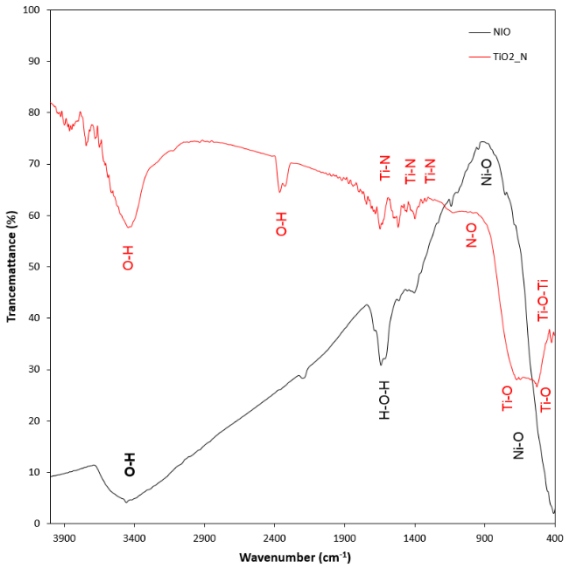

Figure (3) FTIR spectra of TiO_2_N and NiO thin films

Figure (4a) shows the SEM image of N-doped TiO_2 sample as the surface profile and the particle size of the optimal thin film for fabrication of PEC devices were determined. The minimum particle size was found to be 46.89 nm. Homogeneous distribution of nanoparticles can be seen from the SEM image, which can be attributed to the use of magnetron sputtering technique to fabricate nanostructures. In the N-doped TiO_2 samples, the interfacial distance between the nanoparticles indicates an inevitable consequence of the presence of gaseous species (nitrogen) within the structure.

The SEM image of the NiO thin film shown in Fig. (4b) indicates that the minimum particle size is 20.10 nm with homogeneous particle distribution. Figure (5) shows the FE-SEM image of the multilayers structure sample (ITO/N:TiO_2/NiO). The minimum particle size is about 35nm. When compared with the SEM results of individual NiO and N-doped TiO_2 samples, the surface morphology of the multilayers sample is similar to that of the N-doped TiO_2 sample. This can be attributed to the larger particle size of N-doped TiO_2 sample, while the smaller NiO nanoparticles locate in the spaces between the larger particles. If this is the case, then assuming the formation of heterogeneous nanostructures could be reasonably feasible. Such

assumption encourages the synthesis of nanodevices with ferroelectric properties. When compared to conventional thin film structures (NiO/TiO_2) [32], the efficiency of the multilayers structures is higher by 1000%. Accordingly, a drastic development in applications can be expected with more control over the size and distribution of nanoparticles.

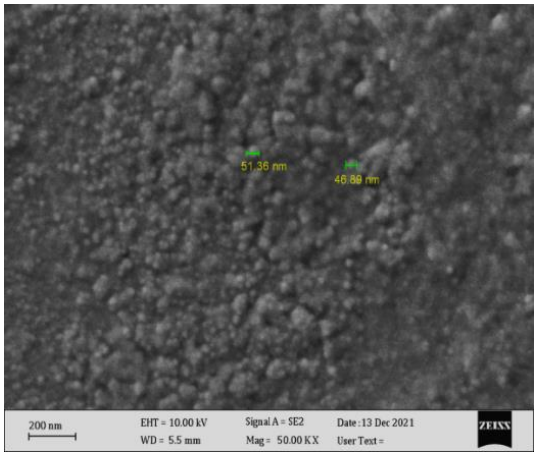

(a)

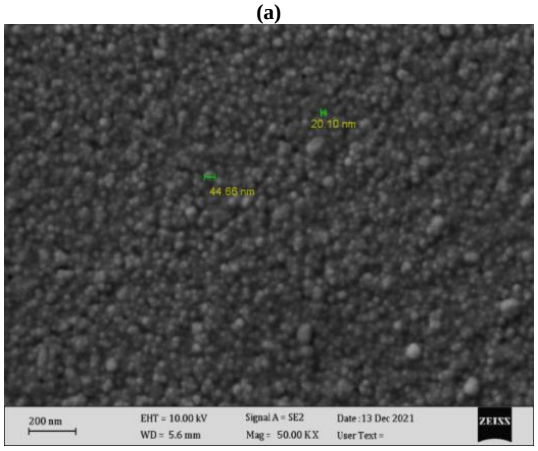

(b)

Fig. (4) SEM images of (a) N-doped TiO_2 thin film, and (b) NiO thin film prepared in this work

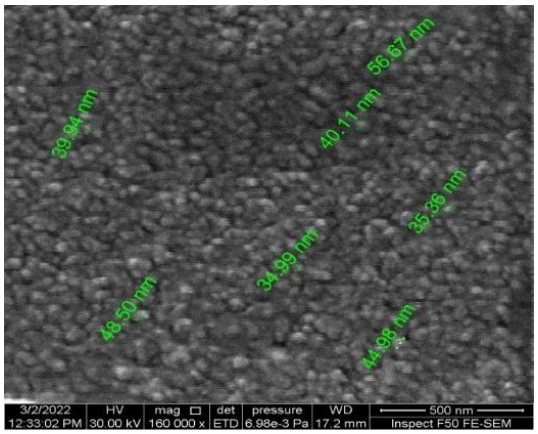

Fig. (5) FE-SEM image of multilayers sample (ITO/N:TiO_2/NiO)

The energy-dispersive x-ray (EDX) spectra of the prepared samples (N-doped TiO_2, NiO and multilayers (ITO/N:TiO_2/NiO) were recorded and analyzed as shown in Fig. (6). A summary of elemental compositions in the final samples is presented too.

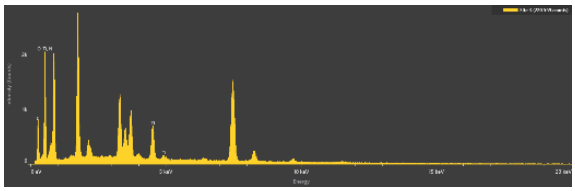

Table (1) EDX analysis of N-doped TiO_2 sample

Element	Atomic %	Atomic % Error	Weight %	Weight % Error
C	23.9	0.5	18.1	0.4
N	9.8	1.2	8.7	1.0
O	63.4	0.9	64.2	0.9
Ti	3.0	0.1	9.0	0.2

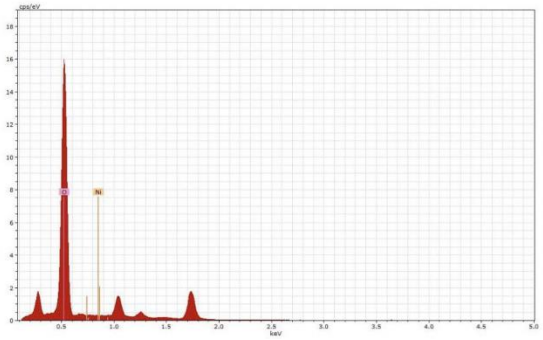

Table (2) EDX analysis of NiO sample

Element	line type	Weight %	Atomic %	Net Int.
O	K series	97.97	99.39	12.13
Ni	K series	2.21	0.61	0.66

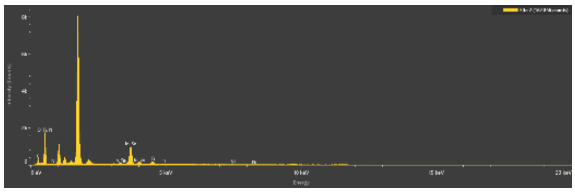

Table (3) EDX values of multilayers sample (ITO/N:TiO_2/NiO)

Element	Atomic %	Atomic % Error	Weight %	Weight % Error
C	13.5	0.5	9.2	0.4
N	4.9	0.5	4.0	0.4
O	78.5	0.7	71.6	0.7
Ti	1.3	0.0	3.5	0.1
Ni	0.1	0.0	0.2	0.1
In	0.8	0.1	5.1	0.5
Sn	0.9	0.0	6.4	0.3

Fig. (6) EDX results of thin film samples prepared in this work: N-doped TiO_2, NiO, and multilayers (ITO/N:TiO_2/NiO)

Figure (7a) shows the transmission spectra of N-doped mixed-phase TiO_2 thin films in the UV and visible regions. These thin films were prepared using different ($Ar:O_2:N_2$) gas mixing ratios of 40:40:20,

60:30:15, 43:42:11, and 76:19:05 after deposition time of 2 hours. These results show that the transmittance decreases with increasing the ratio of nitrogen gas in the gas mixture. The lowest transmittance was obtained for the sample prepared using the mixing ratio of 43:42:15, while the highest transmittance was obtained when mixing ratio of 76:19:05 was used. Figure (7b) shows the transmission spectra of NiO thin films in the UV and visible regions. These films were prepared using a 50:50 mixing ratios of Ar and O_2, respectively, after different deposition times (2, 3 and 4 hours). These results show a decrease in the transmittance as the deposition time got longer. Also, the transmittance was decreased to its minimum value at the edge of UV region.

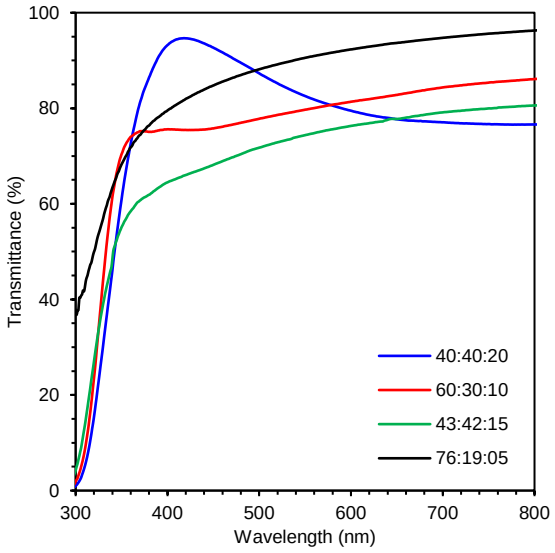

Fig. (7) Transmission spectra of thin film samples prepared in this work (a) N-doped TiO_2, and (b) NiO

The energy band gap of the N-doped TiO_2 thin film samples was determined from the relationship between $(\alpha h\nu)^{1/2}$ and photon energy ($h\nu$). The indirect energy band gap of the N-doped TiO_2 samples prepared using gas mixing ratios of 40:40:20, 60:30:15, 43:42:11, and 76:19:05 are 3.05, 3.18, 3.32, and 3.36 eV, respectively. The energy band gap was decreased with increasing nitrogen content in the sample due to the existence of nitrogen impurities into the TiO_2 matrix. Consequently, this has improved the electronic transitions [33]. Similarly, the energy band gap of the NiO thin film samples prepared after different deposition times (2, 3 and 4 hours) was determined from the relationship between $(\alpha h\nu)^{1/2}$ and photon energy ($h\nu$). These results confirm a decrease in the indirect optical energy band gap with increasing deposition time. The values of energy band gap were 3.1, 3.13 and 3.36 eV corresponding to deposition times of 2, 3 and 4 hours, respectively. This decrease in the band gap can be attributed to the increased content of gases in the sample due to increasing crystal defects or impurities. This leads to the band tailing of the valence and conduction bands and contributes to the band gap narrowing [34].

Figure (8) shows the relation between transmittance and wavelength for optimum samples prepared at different conditions. These results indicate high transmittance of the ITO substrate with a decrease in transmittance when it was covered with a thin film of N-doped TiO_2. In case of multilayers of ITO, N-doped TiO_2 (prepared using gas mixture of 76:19:5 after deposition time of 2 hours), and NiO (prepared using gas mixture of 50:50 after deposition time of 3 hours), the results confirm a dramatic change in transmittance as it decreased to the lowest value at wavelength of 520 nm. To study the photoelectrochemical effect, the ITO, N-doped TiO_2 sample is used as the working electrode and platinum foil as the counter electrode. The electrodes were electrochemically cycled in electrolytes consisting of 1M KOH. Connecting the sample to the negative end of the power supply and the platinum electrode to the positive end, then irradiating the sample with a xenon lamp, the results indicate a decrease in transmittance to the lowest value (see the colored curve). However, connecting the sample to the positive end of the power supply and the platinum electrode to the negative end, the transmittance was increased again (see the bleached curve). The coloration process of the sample corresponds to the oxidation state of metal oxide ions (before the oxygen evolution reaction) while the bleaching process is related to the reduction state of metal oxide ions. The results of the current work are in agreement to those achieved by other works [35,36].

Moreover, after using N-doped TiO_2, the results indicate a decrease in the transmittance of the sample when NiO is deposited over the N-doped TiO_2 layer, as shown in Fig. (8). Also, connecting ITO/N:TiO_2/NiO to the negative end and the platinum electrode to the positive end then irradiation with a xenon lamp, the results indicate a high decrease in

transmittance (see the colored curve). However, by reversing the electrodes, the transmittance increases again (see the bleached curve). At color condition, the results confirm a decrease in the transmittance to 23% when voltages of ±3.4 V were applied with xenon-light irradiation.

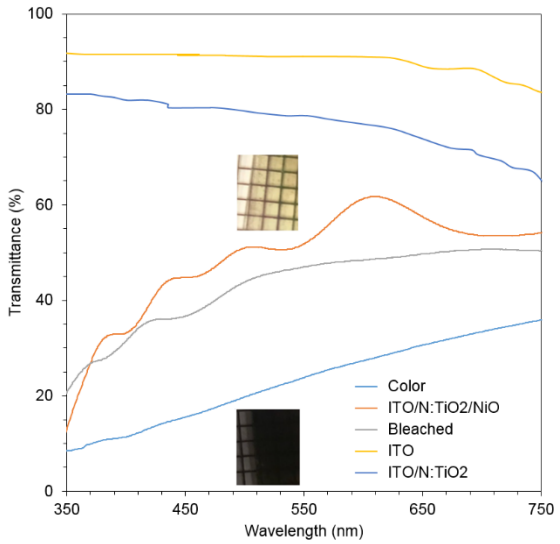

Fig. (8) Transmission spectra of multilayers configuration (ITO/N:TiO_2/NiO) prepared in this work. The photographs of the ITO/N:TiO_2/NiO film with a size of 2×2 cm^2 in the colored and bleached states

4. Conclusions

A modification in the structure of TiO_2 as EC layer is achieved by doping it with nitrogen and thus the ability of using this layer in the PEC device. Multilayers configuration based on ITO/N:TiO_2/NiO was successfully synthesized and tested where both EC (N-doped TiO_2) and IS (NiO) layers are prepared with high optical homogeneity by dc sputtering technique. A decrease in the transmittance to 23% was achieved when voltages of ±3.4 V were applied with xenon-light irradiation. This gives an indication on the efficiency of the PEC device.

References

[1] G.B. Smith, "Green Nanotechnology", SPIE Proc. 8104: "Nanostructured Thin Films IV" 810402 (2011) 9-22.
[2] J. García-Martinez (Ed.), "Nanotechnology for the Energy Challenge", 2nd ed., Wiley-VCH (Weinheim, 2013).
[3] F. Pacheco-Torgal, M.V. Diamanti, A. Nazari, C.G. Granqvist (Eds.), "Nanotechnology in Eco-efficient Construction", Woodhead Publishing (Cambridge, 2013), 1-9.
[4] G. Atak and Ö.D. Coşkun, "Annealing effects of NiO thin films for all-solid-state electrochromic devices", Solid State Ionics, 305 (2017) 43-51.
[5] H. Moulki et al., "Electrochromic performances of nonstoichiometric NiO thin films", Thin Solid Films, 553 (2014) 63-66.
[6] R.T. Wen et al., "Anodic electrochromism for energy-efficient windows: cation/anion-based surface processes and effects of crystal facets in nickel oxide thin films", Adv. Func. Mater., 25(22) (2015) 3359-3370.
[7] Q. Liu et al., "Charge-transfer kinetics and cyclic properties of inorganic all-solid-state electrochromic device with remarkably improved optical memory", Solar Energy Mater. Solar Cells, 174 (2018) 545-553.
[8] K. Zhou et al., "The influence of crystallinity on the electrochromic properties and durability of NiO thin films", Surf. Interfaces, 6 (2017) 91-97.
[9] P. Yang, P. Sun and W. Mai, "Electrochromic energy storage devices", Mater. Today, 19(7) (2016) 394-402.
[10] F.J. Al-Maliki and E.A. Al-Oubidy, "Effect of gas mixing ratio on structural characteristics of titanium dioxide nanostructures synthesized by DC reactive magnetron sputtering", Physica B: Cond. Matter, 555 (2019) 18-20
[11] J.M. Wang, W.S. Xiao and J. Zhihui, "Application of nanostructures in electrochromic materials and devices: recent progress", Materials, 3 (2010) 5029-5053.
[12] L. Zhu, "Development of Metal Oxide Solar Cells through Numerical Modeling", Ph.D. thesis, University of Bolton, (2012).
[13] D.G. Colombo et al., "Anhydrous metal nitrates as volatile single source precursors for the CVD of metal oxide films", Chem. Vapor Deposi., 4(6) (1998) 220-222.
[14] P. Bezerra et al., "Synthesis, characterization, and photocatalytic activity of pure and N-, B-, or Ag-doped TiO_2", J. Braz. Chem. Soc., 28(9) (2017) 1788-1802.
[15] O.A. Hammadi, F.J. Al-Maliki and E.A. Al-Oubidy, "Photocatalytic activity of nitrogen-doped titanium dioxide nanostructures synthesized by dc reactive magnetron sputtering technique", Nonl. Opt. Quantum Opt.: Concepts in Modern Optics, 51(1-2) (2019) 67-78.
[16] Y. Chen and K. Liu, "Preparation of granulated N-doped TiO_2/diatomite composite and its applications of visible light degradation and disinfection", Powder Technol., 303 (2016) 176-191.
[17] F.J. Al-Maliki, O.A. Hammadi, B.T. Chiad and E.A. Al-Oubidy, "Enhanced photocatalytic activity of Ag-doped TiO_2 nanoparticles synthesized by DC Reactive Magnetron Co-Sputtering Technique", Opt. Quantum Electron., 52 (2020) 188.
[18] R.A.H. Hassan and F.T. Ibrahim, "Preparation and Characterization of Ni-doped TiO_2 Nanostructures for Surface Cleaning Applications", Iraqi J. Appl. Phys., 17(1) (2021) 3-8.
[19] L. Zhang et al., "N-TiO_2-coated polyester filters for visible light – Photocatalytic removal of gaseous toluene under static and dynamic flow conditions", J. Environ. Chem. Eng., 4(1) (2016) 357-364.

[20] O.A. Hammadi, M.K. Khalaf and F.J. Kadhim, "Fabrication of UV Photodetector from Nickel Oxide Nanoparticles Deposited on Silicon Substrate by Closed-Field Unbalanced Dual Magnetron Sputtering Techniques", Opt. Quantum Electron., 47(12) (2015) 3805-3813.
[21] S.Y. Park et al., "Organic solar cells employing magnetron sputtered p-type nickel oxide thin film as the anode buffer layer", Solar Energy Mater. Solar Cells, 94(12) (2010) 2332-2336.
[22] S.I. Park et al., "A review on fabrication processes for electrochromic devices", Int. J. Precision Eng. Manuf. – Green Technol., 3 (2016) 397-421.
[23] J. He et al., "Facile formation of anatase/rutile TiO_2 nanocomposites with enhanced photocatalytic activity", Molecules, 24(16) (2019) 2996.
[24] Q. Guo et al., "Synthesis of uniform titanium nitride nanocrystalline powders via a reduction–hydrogenation–dehydrogenation–nitridation route", J. Amer. Cer. Soc., 88(1) (2005) 249-251.
[25] M.F.C. Ladd and R.A. Palmer, "Structure determination by X-ray crystallography", 5th ed., Springer (NY, 1977).
[26] F.J. Al-Maliki, O.A. Hammadi and E.A. Al-Oubidy, "Optimization of Rutile/Anatase Ratio in Titanium Dioxide Nanostructures prepared by DC Magnetron Sputtering Technique", Iraqi J. Sci., 60(special issue) (2019) 91-98.
[27] B.E. Warren, "X-ray Diffraction", Courier Corporation (NY, 1990) p. 253.
[28] H. Qiao et al., "Preparation and characterization of NiO nanoparticles by anodic arc plasma method", J. Nanomater., (2009) article ID 795928.
[29] F.J. Al-Maliki and N.H. Al-Lamey, "Synthesis of Tb-doped titanium dioxide nanostructures by sol–gel method for environmental photocatalysis applications", J. Sol-Gel Sci. Technol., 81 (2017) 276-283.
[30] Y. Huo et al., "Highly active $TiO_{2-x-y}N_xF_y$ visible photocatalyst prepared under supercritical conditions in NH_4F/EtOH fluid", Appl. Catal. B, Environmental, 89(3-4) (2009) 543-550.
[31] B. Anandan and V. Rajendran, "Morphological and size effects of NiO nanoparticles via solvothermal process and their optical properties", Mater. Sci. Semicond. Process., 14(1) (2011) 43-47.
[32] R.H. Turki and M.A. Hameed, "Spectral and Electrical Characteristics of Nanostructured NiO/TiO_2 Heterojunction Fabricated by DC Reactive Magnetron Sputtering", Iraqi J. Appl. Phys., 16(3) (2020) 39-42.
[33] H. Liu et al., "Nitrogen-doped black TiO_2 spheres with enhanced visible light photocatalytic performance", SN Appl. Sci., 1 (2019) article no. 487.
[34] S.U. Awan et al., "Defects induced luminescence and tuning of bandgap energy narrowing in ZnO nanoparticles doped with Li ions", J. Appl. Phys., 116(8) (2014) 083510.
[35] G. Cai et al., "Constructed TiO_2/NiO core/shell nanorod array for efficient electrochromic application", J. Phys. Chem. C, 118(13) (2014) 6690-6696.
[36] M.A. Hameed, S.H. Faisal, R.H. Turki, "Characterization of Multilayer Highly-Pure Metal Oxide Structures Prepared by DC Reactive Magnetron Sputtering Technique", Iraqi J. Appl. Phys., 16(4) (2020) 25-30

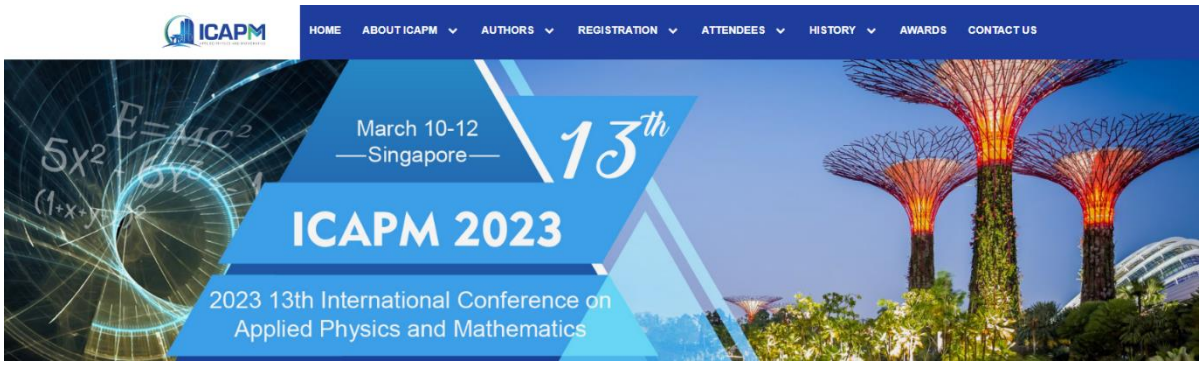

In the past 12 years, ICAPM was held in large capital cities, such as Tokyo, Phuket, Singapore, Busan, Lisbon, and Hong Kong, Bangkok, etc. It has become a very important international platform. We are looking forward to meeting you at this momentous occasion to discuss research and challenges again!

2023 13th International Conference on Applied Physics and Mathematics (ICAPM 2023) will be held in Singapore during March 10-12, 2023. This conference will provide a remarkable opportunity for the academic and industrial communities to address new challenges and share solutions, and discuss future research directions. Contributions are expected from academia, industry, and management agencies.

ICAPM 2023 welcomes author submission of papers concerning any branch of the Applied Physics and Mathematics, and their applications in education, and other subjects. The subjects covered by ICAPM 2023 include Advances in Instrumentation and Techniques Applications of Microscopy in the Physical Sciences and their applications.

PROCEEDINGS

IOP Publishing

After double-blind reviewing, accepted and presented papers will be published by *ICAPM 2023 Proceedings- IOP Journal of Physics: Conference Series*, which is indexed by ISI Web of Science (Conference Proceedings Citation Index), Scopus, Ei Compendex, etc.

Submit now:

https://www.zmeeting.org/submission/icapm2023

Submitted paper will be peer reviewed. All accepted papers will be published into ICAPM 2023 Conference Proceedings, which will be published through the IOP Journal of Physics: Conference Series. IOP Conference Series is an open-access proceeding publication indexed by ISI Web of Science (Conference Proceedings Citation Index), Scopus, Ei Compendex, etc.

The conference is soliciting state-of-the-art research papers in the following areas of interest:

Advances in Instrumentation and Techniques
Applications of Microscopy in the Physical Sciences
Applied Materials Science & Engineering
Applied Non-linear Physics
Applied Optics, Non-linear optics, Laser Physics, Ultrafast phenomena, Lasers application to Medicine, Chemistry
Applied Solid State Physics/Chemistry and Materials Science and Technology Advanced Materials
Astrophysics and Plasma Physics
Atomic, Molecular and Chemical Physics
Biomaterials Science and Biomedical Engineering
Biomedical Engineering, Medical/Biological Physics, Health Physics, Biomechanics
Biophysics, Bio (electro) magnetism, Biophysical Chemistry
Complex systems
Computational Physics, Non-linear Physics
Condensed Matter Physics
Condensed Matter Physics and Materials Science
Engineering and Industrial Physics, Instrumentation, Metrology and Standards
Environmental Physics
Imaging Techniques, Microscopy
Large-code development
Medical Physics
Methodological advances
Nanoscale physics
Nanoscience and Nanotechnology
Nanoscience and Nanobiotechnology
Non-equilibrium systems
Nuclear Physics/Chemistry, Radioactivity, Radiochemistry, Radiation Safety
Nuclear Sciences and Engineering
Particle Physics
Petascale computing
Physical Chemistry
Physical Properties of Biological/Biomedical Systems through Microscopy
Plasma physics
Polymers
Optical Physics, Quantum Electronics and Photonics
Quantum Physics
Quantum Monte Carlo
Radiation Physics, Radiation Chemistry, Radiation Processing, Radiation-Matter interaction, Spectroscopies
Radioactivity and Radiochemistry, Radiation Protection and Safety Issues
Semiconductors devices and Photonics, Opto-electronics, Quantum Electronics
Soft and granular matter
Solid State Physics
Surfaces, Interfaces and Colloids

Applied Mathematics and Engineering: Modeling, Analysis and Computation
Applied partial differential equations
Numerical analysis and methods
Scientific computation
Mathematical methods in optics and electromagnetics
Mathematical modeling in materials science and biology
Nonlinear problems in mechanics
Homogenisation and multiscale analysis
Inverse problems
Algebra and its application
Differential equations, dynamical systems and their applications
Engineering applications and scientific computations
Financial and actuary mathematics
Fuzzy mathematics and its applications
Geometry and its application
Modeling and simulation
Statistical methods in technical and economic sciences and practice

IRAQI JOURNAL OF APPLIED PHYSICS
Vol. 18, No. 2, April-June 2022, pp. 19-24

Characterization of Indium Nitride Thin Films Prepared by Plasma-Assisted Molecular Beam Epitaxy

Ali M. Hassan [1]
Peter M. Millner [2]
James G. McAlley [2]

[1] *Department of Medical Physics, Al-Hasseb University College, Najaf, IRAQ*
[2] *Department of Physics, Faculty of Science, Bournemouth University, Bournemouth, UK*

The growth and electronic structure of indium nitride has been presented. Indium nitride thin films were grown by plasma-assisted molecular beam epitaxy (PAMBE). The significance of the relative fluxes, substrate temperature and buffer layers was explored and related to the electrical and structural properties of the prepared films. Alongside the effect of active nitrogen species on indium nitride films, it was found that excited molecular nitrogen was preferred for growth over atomic and ionic species. An optimized recipe for indium nitride was developed incorporating all explored parameters.

Keywords: Indium nitride; Molecular beam epitaxy; Thin films; Electronic structure
Received: 8 April 2022; **Revised:** 29 April 2022; **Accepted:** 06 May 2022

1. Introduction

Epitaxy is defined as the deposition of a monocrystalline film on a monocrystalline substrate, keeping a certain lattice alignment known as epitaxial relationship. The heteroepitaxy is used when the substrate and the epilayer are different materials [1,2]. Heteroepitaxy is the deposition of material A on material B. In this case, various growth modes can be observed, depending on the lattice mismatch between the materials and surface energy: Layer-by-layer growth, also called Frank Van der Merwe growth, Three-dimensional (3D) growth, called Volmer-Weber growth, and Stranski-Krastanov growth [3-5]

High quality epitaxial thin films can be synthesized via chemical vapor deposition (CVD) or physical deposition (Molecular Beam Epitaxy, MBE) [6,7]. In comparison to CVD techniques, MBE presents several advantages which stem from its lower growth temperature and in situ monitoring via Reflection High-Energy Electron Diffraction (RHEED) [8,9]. They are good control of layer thickness, due to a low growth rate (less than one monolayer (ML) per second) and reduced inter-diffusion effects [10]. Also, synthesis of a wide range of ternary or quaternary alloys. Even materials that are barely miscible under thermodynamic equilibrium can be dynamically stabilized by MBE [11]. Finally, higher dopant concentrations thanks to the minimization of segregation effects [12].

In the particular case of III-nitrides, additional advantages can be found, such as the possibility to change the material polarity, depending on the substrate or buffer layer [13,14]. As well, the activation of Mg-dopant is not required, because of the H-free growth environment [15].

The epitaxial growth process depends on the impinging fluxes on the one hand and the substrate temperature on the other hand [16]. The substrate temperature is the key parameter which activates the different phenomena occurring at the growing surface [17].

As can be seen in Fig. (1), the impinging fluxes can be adsorbed at the surface by chemisorption (if chemical bonds are created via a transfer of electrons between impinging atoms and atoms from the surface) or physisorption (if the atoms are adsorbed via Van der Waals forces) [18]. At a given substrate temperature and concentration, the atoms have a certain mobility [19]. Some of the species will diffuse and be desorbed without being incorporated to the layer, whereas the others will incorporate either by step-edge growth forming atomic terraces or by cluster nucleation [20].

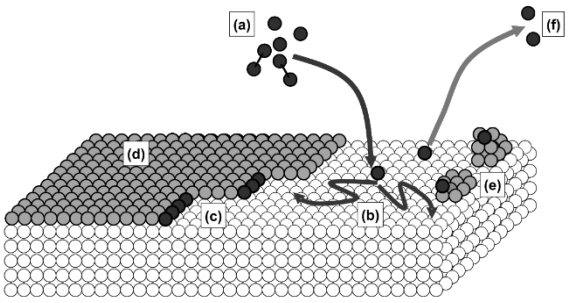

Fig. (1) Atomistic processes that can occur at the surface during the growth: (a) adsorption, (b) diffusion, (c) step-edge growth, (d) atomic terraces, (e) nucleation of clusters and (f) desorption

Techniques that have led to low cost, high density processing of silicon have resulted in silicon integrated circuits becoming ubiquitous within modern society. The astonishing progress which has been achieved in the processing of silicon is encompassed by Moore's law [21,22]. In 1965, only 5 years after the first planar integrated circuit was produced, Gordon Moore noted that the density of

transistors being fabricated on silicon integrated circuits was doubling approximately every 2 years [23]. Remarkably this trend has continued to the present day and the latest generation of microprocessors now pack more than half a billion transistors onto a square centimeter [24,25].

While the ability of semiconductors to rapidly process information may be the most visible application, semiconductors are used in applications as wide reaching as solid state lighting, power distribution, photovoltaics and high speed communications [26-29]. When considering which semiconductor is preferred for a given application a number of material properties must be considered. High frequency devices rely on high peak carrier drift velocities along with compatibility with high-k dielectrics [30]. For light emitting applications, the size and nature of the electronic bandgap must be considered. High power operation requires the material to be relatively insensitive to moderate changes in temperature [31].

The first report of III-nitrides synthesis was in 1938 by Juza et al. who synthesized GaN and InN crystallites [32]. The GaN was formed by flowing ammonia over hot gallium, and the InN from $InF_6(NH_4)_3$ reduction. The purpose of this initial study was to measure lattice parameters of the materials and there was little interest in their optical properties at that stage [33]. It was 30 years later, when Maruska et al. first grew GaN layers by vapor phase deposition on sapphire substrates, that interest in the nitrides increased [34]. Following this report, blue LEDs based on GaN:Zn/n-GaN structures were produced by Pankove et al. on vapor phase grown GaN [35,36]. These structures relied on hot carrier injection from avalanche breakdown to generate holes. Despite subsequent advances in growth, p-type GaN proved elusive and it was not until 1989 when Amano et al. succeeded in reliably producing p-type GaN by Mg doping [37]. Nakamura et al. have utilized Mg doping to form p-n junctions, and at the time, the brightest blue LEDs made from any material system [38]. Akasaki et al. and Nakamura et al. subsequently produced the first laser diodes based on the material system [39,40]. Progress has continued at a remarkable rate, with the number of research groups studying the III-nitrides ballooning [41]. Recent efforts have focused on improving the efficiency of nitride based LEDs and laser diodes and extending the range of wavelengths over which they operate. Added effort has also been applied to HEMTs based on nitride heterojunctions [42]. For a thorough account of the historical developments in the GaN field see the reviews by Jain et al. [43] and Pankove et al. [44].

2. Experimental Work

The nitride MBE system used in this work is a Perkin-Elmer model 430. The water cooled chamber is fitted with ion and cryo pumps (cryo pumped exclusively during film growth) which results in a base pressure of about $5x10^{-11}$ Torr. Active nitrogen is supplied by a radio frequency inductively coupled plasma source, and all metallic species are supplied by standard or high temperature effusion cells. Samples can be transferred in and out of the system using a three chamber load-lock. Growth can be monitored in-situ by a reflection high energy electron diffraction (RHEED) system, and also a custom built laser interferometer. Substrates are mounted on 78 mm molybdenum blocks via indium or indium-tin solder. The growth temperature can be controlled by a high temperature substrate manipulator heater capable of temperatures greater than 1200℃. The substrate manipulator temperature is monitored by a thermocouple touching the back side of the molybdenum block. Growth temperatures were calibrated using a silicon/aluminum eutectic.

As the common form of nitrogen is inert at achievable growth temperatures, a plasma or ion source is required to activate the N_2 molecule. The primary source used in this work was an HD-25 radio frequency inductively coupled plasma source (RF-ICP). An earlier plasma source model, the MDP-21, was used for initial studies. Unless otherwise stated, results refer to growth with the HD-25. All nitrogen which flowed into the RF-ICP was filtered by a nickel inert gas filter, and flow was moderated by a 0-5 sccm mass flow controller. The basic structure of an RF-ICP is shown in Fig. (1).

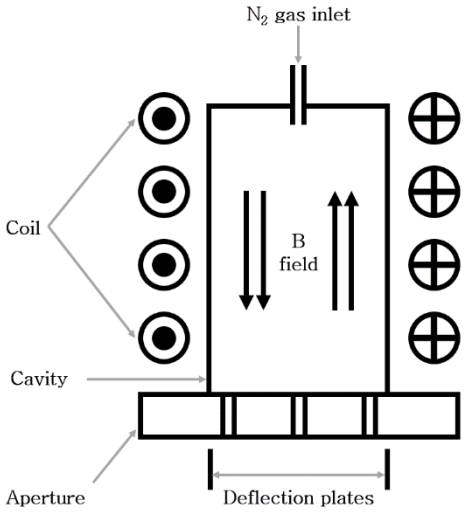

Fig. (1) The main features of a radio frequency inductively coupled plasma source

Nitrogen is controllably leaked into the cavity via the inlet. A water cooled coil couples the RF signal into the cavity via a magnetic field which is most intense at the center of the cavity. The alternating field accelerates charged particles which collide further with other species and a plasma is formed. Typically the source (both HD-25 and MDP-21) was operated at RF powers of 150-350 W and a flow rate

of 1.3 sccm for film growths. The species generated by an RF-ICP can vary substantially at different plasma operating conditions and also from different source geometries.

A number of post growth characterization techniques are discussed within this chapter. It is not feasible to give a comprehensive overview of each technique, so only a brief technique summary is given here along with key operating parameters. The reader is directed to the thorough review of semiconductor characterization techniques [45] for further information.

3. Results and Discussion

In order to map out the different growth regimes for the MBE system, two GaN films were grown with the Ga flux varied in discreet steps. The nitrogen plasma conditions were unchanged during growth and the growth rate was measured at the various flux ratios by laser interferometry using a semiconductor laser operating at 658 nm. The films were both grown on sapphire substrates at 700°C with a low temperature GaN buffer grown at 500°C. Figure (2) shows the growth rate of the two GaN films grown at RF powers of 350 W and 150 W, respectively.

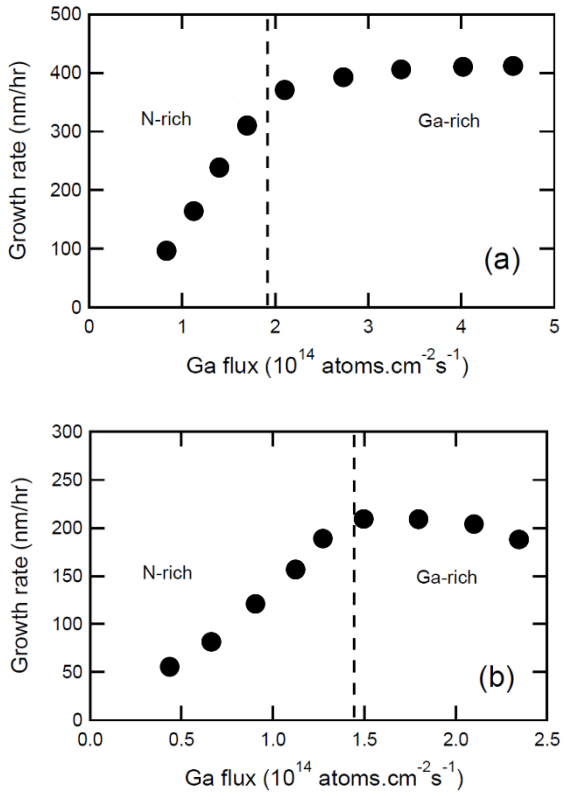

Fig. (2) The growth rate of GaN layers at various Ga fluxes. (a) Ga-polar GaN with plasma RF power of 350 W and flow rate of 1.3 sccm. (b) N-polar GaN with plasma RF power of 150 W and flow rate of 1.3 sccm. The dashed line represents the Ga flux where the growth rate begins to saturate, this point marks the transition between the N-rich and Ga-rich regimes

A constant nitrogen flow rate of 1.3 sccm was used for both films. As we can see from Fig. (3), no intermediate regime exists at growth temperatures of 700°C. This indicates that the saturation in growth rate in both figures (2a) and (2b) marks the transition between N-rich and Ga-rich conditions. Increasing the RF power shifts the transition between the two regimes to higher Ga flux. By using these plots it was possible to choose a Ga flux that was slightly into the Ga-rich regime. This corresponded to a Ga flux of 2.1 and $1.5x10^{14}$ atoms/cm^2.s for the 350 and 150 W plasma measurements, respectively. This Ga flux was then used for future optimized GaN films and buffer layers. It should be noted that the laser interferometry technique became available only towards the end of this thesis and originally the transition to the Ga-rich regime had been determined by observing the presence of Ga droplets on film surfaces. This original approach yielded a Ga flux within 5% of the laser interferometry determined Ga flux for the boundary between the two regimes.

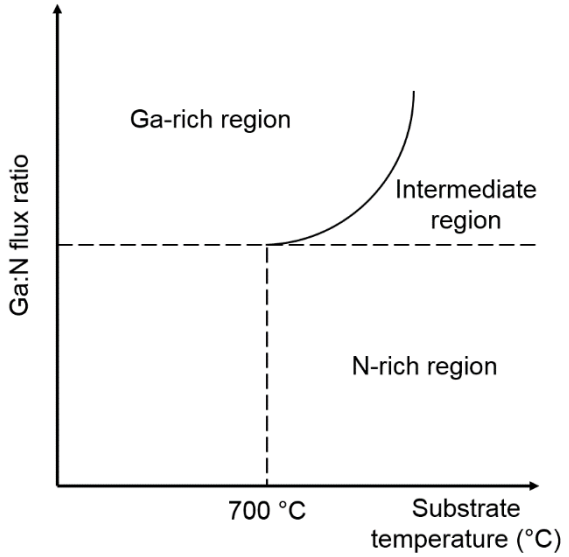

Fig. (3) The GaN growth diagram indicating the three conditions which MBE grown GaN can be produced

The polarity of GaN films has been shown to strongly influence film properties. Typically GaN films grown on sapphire by MBE are N-polar, while films grown on sapphire by MOCVD are Ga-polar. The Ga-polar surface has been shown to be the preferred surface for high quality GaN growth [46,47]. Often AlN buffer layers are employed to achieve the Ga-polar growth mode in MBE growth [48]. The other common technique used to achieve Ga-polar growth by MBE is to use an MOCVD grown GaN template as the substrate. In this work GaN layers were grown on sapphire and MOCVD GaN templates to achieve N-polar and Ga-polar layers, respectively. Films were grown on both substrates under Ga-rich and N-rich flux conditions. No nitridation step was used. Films had a 50 nm low

temperature buffer layer grown at 500°C, and then a 400 nm high temperature layer grown at 700°C. Figure (4) shows AFM images of the four films, along with the root mean square (rms) roughness of each film.

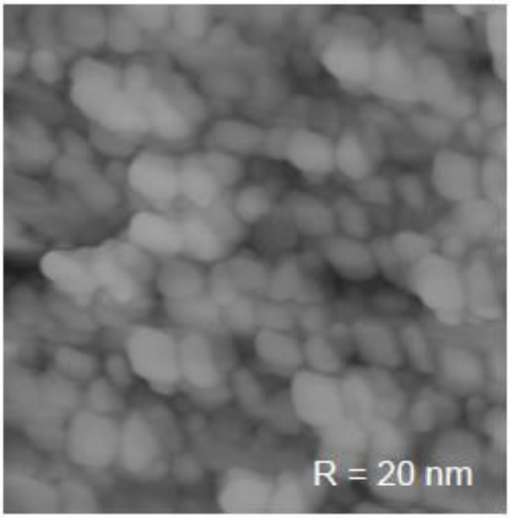

N-polar, Ga-rich

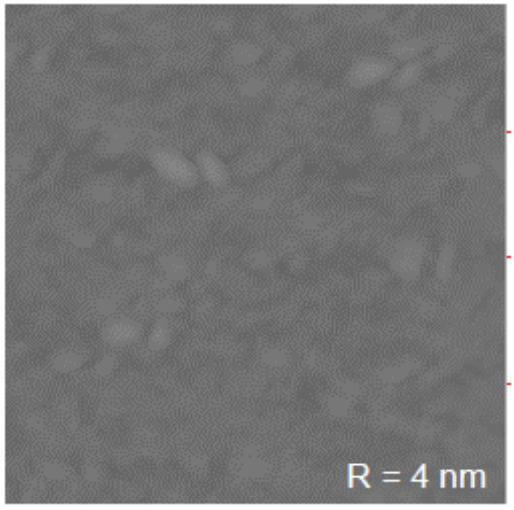

Ga-polar, Ga-rich

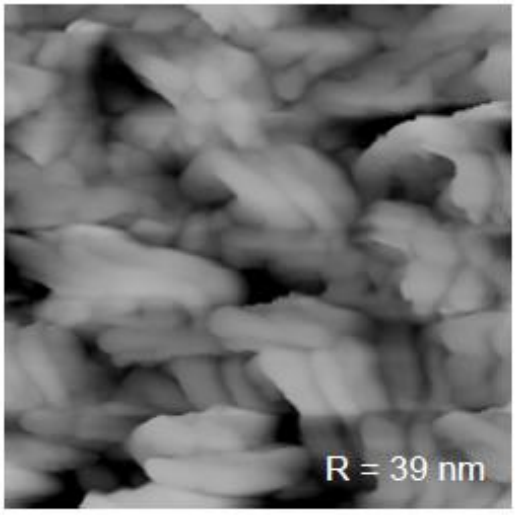

N-polar, N-rich

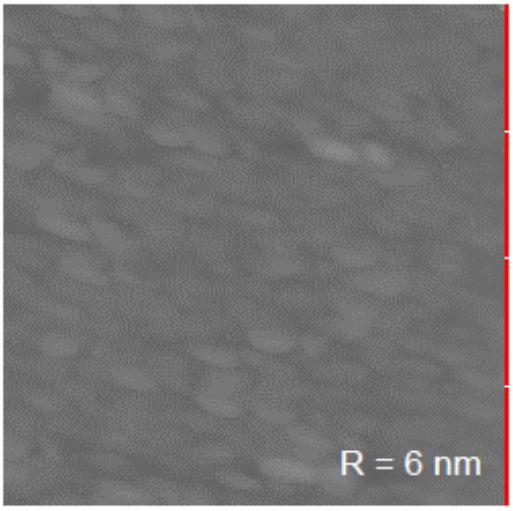

Ga-polar, N-rich

Fig. (4) AFM images of N-polar and Ga-polar GaN films grown in both the Ga-rich and N-rich regimes. R is the root mean square surface roughness

Clearly the films grown on the GaN templates have much flatter morphologies, a result of the films growing homoepitaxially on an already relaxed GaN template. The films grown on sapphire, on the other hand, are highly strained due to the large lattice mismatch of GaN on sapphire. Additionally, the films grown on sapphire are expected to be N-polar as opposed to the preferred Ga-polarity of the MOCVD templates. The films grown in the Ga-rich regime show a small improvement in surface roughness, although the effect is small compared to the effect of the polarity and lattice mismatch.

From an InN perspective, the interest in GaN growth extends only as far as it can assist in producing improved InN films. As a buffer layer for InN, the GaN must be of high structural quality, indicating that growth in the Ga-rich regime with Ga-polarity should be preferred. We also want the GaN to be as electrically insulating as possible so that the buffer layers do not distort electrical measurements we make on InN layers. Hall effect measurements on all GaN films revealed that the GaN layers had high resistivity. It was often difficult to obtain reliable Hall data as the currents achieved through the GaN layers were small. Carrier concentrations below 10^{18} cm^{-3} were common. Hall mobilities <10 $cm^2/V.s$ were measured for non-optimized films, and up to 150 $cm^2/V.s$ for optimized growth.

4. Conclusions

Indium nitride has been a very challenging material to grow with structural and electrical characteristics considered “high quality” by the electronics community. In particular, the limitations on growth temperature imposed by the dissociation of the material is a major hinderance. The growth regimes of the material were found to follow similar

trends to the closely related GaN material system, with growth close to the "In-rich" regime preferred over growth at low In:N ratios.

References

[1] E.G. Bauer et al., "Fundamental issues in heteroepitaxy — A Department of Energy, Council on Materials Science Panel Report", J. Mater. Res., 5 (1190) 85.
[2] M. Ohring, **"The Materials Science of Thin Films"**, Academic Press (San Diego, 1992) 197.
[3] T.K. Chu and A. Martinez, "Epitaxial IV-VI Semiconductor Films", MRS Online Proc. Lib, 90 (1986) 59.
[4] J. Jacob et al., "Correlating in situ RHEED and XRD to study growth dynamics of polytypism in nanowires", Nanoscale, 13 (2021) 13095-13107.
[5] D.S. McPhail, "Applications of Secondary Ion Mass Spectrometry (SIMS) in Materials Science", J. Mater Sci., 41 (2006) 873-903.
[6] C. Lamberti, "The use of synchrotron radiation techniques in the characterization of strained semiconductor heterostructures and thin films", Surf. Sci. Rep., 53(1-5) (2004) 1-197.
[7] G. Li and C. Jagadish, "Recent progress in δ-doping of III–V semiconductors grown by metal organic vapour phase epitaxy", Sol. Stat. Electron., 41(9) (1997) 1207-1225.
[8] S. Angizi et al., "A comprehensive review on planar boron nitride nanomaterials: From 2D nanosheets towards 0D quantum dots", Prog. Mater. Sci., 124 (2022) 100884.
[9] L.-Q. Chen and Y. Zhao, "From classical thermodynamics to phase-field method", Prog. Mater. Sci., 124 (2022) 100868.
[10] C. Garlisi et al., "Multilayer thin film structures for multifunctional glass: Self-cleaning, antireflective and energy-saving properties", Appl. Ener., 264 (2020) 114697.
[11] L.A. Walsh et al., "Molecular Beam Epitaxy of Transition Metal Dichalcogenides" in **Molecular Beam Epitaxy**, 2nd ed., M. Henini (ed.) (2018) Ch. 22, 515-531.
[12] N.E. Richey, C. de Paula and S.F. bent, "Understanding chemical and physical mechanisms in atomic layer deposition", J. Chem. Phys., 152 (2020) 040902.
[13] J. Zúñiga-Pérez et al., "Polarity in GaN and ZnO: Theory, measurement, growth, and devices", Appl. Phys. Rev., 3 (2016) 041303.
[14] T.F. Kuech, S.E. Babcock and L. Mawst, "Growth far from equilibrium: Examples from III-V semiconductors", Appl. Phys. Rev., 3 (2016) 0404801.
[15] J.J. Meindl, "Beyond Moore's Law: the interconnect era", Comput. Sci. Eng., 5(1) (2003) 20-24.
[16] A.A. Demkov et al., "Materials for emergent silicon-integrated optical computing", J. Appl. Phys., 130 (2021) 070907.
[17] A. Yu, "The Future of Microprocessors", IEEE Micro, 16(6) (1996) 46-53.
[18] P. Zhang et al., "100 years of the physics of diodes", Appl. Phys. Rev., 4 (2017) 011304.
[19] T.Y. Kim, W. Suh and U. Jeong, "Approaches to deformable physical sensors: Electronic versus iontronic", Mater. Sci. Eng.: R: Reports, 146 (2021) 100640.
[20] A. Talaat et al., "Review on soft magnetic metal and inorganic oxide nanocomposites for power applications", J. Alloys Comp., 870 (2021) 159500.
[21] A. Balmer et al. "Oxide-defined GaSb VCSELs on ITO substrates", *J. Photon. Technol.*, 11 (1999) 33-36.
[22] C. Dwight et al. "Integration of III-V optoelectronic devices with Si-based circuitry", *Opt. Res. Lett.*, 13 (2001) 55-56.
[23] E. Fowler et al. "Bubble-Free Germanium Wafer Bonding in a Non-Cleanroom Ambient", *Czech J. Phys.*, 15 (2003) 67-70.
[24] G. Heinrisch et al. "Nickel contamination and indium segregation in directly bonded silicon wafers", *J. Solid Stat. Opt.*, 17 (2005) 81-84.
[25] I. Jafaar et al. "Bonding of silicon wafer by novel design of monolayers", *Acta Mater.*, 10 (2007) 103-106.
[26] K. Lancer et al. "Surface activation of silicon wafer bonding at low temperatures", *Mater. Commun.*, 12 (2009) 21-24.
[27] M. Neumann et al. "Room-temperature semiconducting wafer bonding in high vacuum environment", *J. Solid Stat. Technol.*, 8 (2012) 39-42.
[28] O. Parker et al. "Fusion bonding of oxidized silicon wafers at low temperatures", *Solid Stat. Lett.*, 14 (2015) 57-60.
[29] Q. Ronahi et al. "Fusion bonding of silicon wafers in low vacuum", *Solid Stat. Lett.*, 15 (2016) 113-116.
[30] S. Tucker et al. "Fusion bonding of silicon wafers with polymer thin films at room temperature", *Acta Mater.*, 13 (2010) 207-210.
[31] U. Vlahovich et al. "Low-dark-current wafer-bonded Si/InSb photodiodes", *J. Photon. Technol.*, 17 (2005) 311-314.
[32] W. Xu et al. "Fusion-bonded InSb wafers for photonics networks", *Opt. Res. Lett.*, 22 (2010) 125-128.
[33] Y. Zhang et al. "Room-temperature fusion bonding technology for photonics networks", *Opt. Res. Lett.*, 23 (2011) 103-106.
[34] A. Zahidi et al. "Chemical cleaning of InSb(100) surfaces in HF solutions", *Opt. Mater. Lett.*, 26 (2004) 13-16.

[35] Y. Bond et al. "Chemical cleaning of GaSb(100) surfaces in aqueous solutions", *Opt. Mater. Lett.*, 27 (2005) 215-218.
[36] C. Xiao et al. "SIMS analysis of HF/UV treated silicon (100) surfaces", *Solid Stat. Lett.*, 18 (2019) 69-72.
[37] W. Dillan et al. "Ohmic conduction across wafer-bonded compound semiconducting interfaces", *Acta Mater.*, 22 (2019) 441-444.
[38] E. Varner et al. "Self-propagating low-temperature germanium wafer bonding", *Solid Stat. Lett.*, 21 (2021) 355-358.
[39] U. Fitzgerald et al. "High bonding energy and thermal stress in silicon on ITO wafer bonding", *Solid Stat. Lett.*, 21 (2021) 467-470.
[40] G. Tayeb et al. "Hetero-interface silicon photodetector with high gain-bandwidth-product", *Opt. Res. Lett.*, 32 (2021) 327-330.
[41] S. Hömels et al. "Direct wafer bonding for super-junction fabrication", *Photon. Opto. Lett.*, 19 (2020) 143-146.
[42] I. Reynolds et al. "Non-destructive measurements of wafer-bonded surface energy", *Photon. J. Photon. Technol.*, 31 (2019) 1219-1222.
[43] Q. Jong et al. "Electrical characteristics of CdS/Si heterojunction solar cells under radiation effect", *J. Photon. Technol.*, 25 (2020) 129-132.
[44] K. Poles et al. "Fabrication of CdS/Si heterojunction solar cells by chemical bath method", *Solid Stat. Lett.*, 20 (2020) 277-280.
[45] O. Leon et al. "Deposition of CdSe thin films on ITO substrates by PLD method", *Prog. Mater. Phys.*, 12 (2018) 45-48.
[46] M. Nabawi et al. "Wafer-bonding fabrication of InSb/InP heterostructures on silicon substrates", *Prog. Mater. Phys.*, 13 (2019) 123-126.
[47] N. Müller et al. "Wafer-bonding of InGaP thin films on (100) silicon substrates", *Prog. Mater. Phys.*, 14 (2020) 257-260.
[48] L. Omran et al. "Wafer-bonding of InGaSb thin films on (100) silicon substrates", *Prog. Mater. Phys.*, 15 (2021) 369-372.

IRAQI JOURNAL OF APPLIED PHYSICS
Vol. 18, No. 2, April-June 2022, pp. 25-30

Optimized Characteristics of Silver Nanoparticles Synthesized by Chemical Reduction and Embedded in Silica Xerogels

Tabarak A. Al-Mashhadani
Firas J. Al-Maliki

Department of Physics, College of Science, University of Baghdad, Baghdad, IRAQ

In this work, silica xerogel doped with silver nanoparticles has been prepared via sol-gel route at specific preparation parameters. Spherical and uniform silver nanoparticles (Ag NPs) had been prepared by chemical reduction method in silver nitrate aqueous precursor using trisodium citrate as reducing agent at boiling temperature. The minimum crystallite size in the range of 15-33 nm was produced .The structural and optical characteristics were determined as functions of the concentration and reduction period. According to the results of field-emission scanning electron microscopy (FE-SEM), the particle size of Ag NPs was increased with increasing reduction period and concentration. Also, the influences of these parameters on the particle size as well as on the characteristic surface plasmon absorption band were determined and studied at 420±30 nm. The broadening of the surface plasmon resonance (SPR) band indicated the existence of larger particles in the solution. The absorption intensity was reasonably increased in case of the bulk samples (Ag NPs in xerogels) when compared to that of Ag NPs in the solution. The final solid samples of Ag NPs in silica xerogels can be successfully used as catalyst for white-emission photoluminescence of rare earth elements.

Keywords: Ag NPs; Silica xerogel; Chemical reduction; Surface plasmon resonance
Received: 17 May 2022; Revised: 18 July 2022; Accepted: 25 July 2022

1. Introduction

Due to its unusual tunable optical properties, silver nanoparticles (Ag NPs) are one of the noblest and most widely explored metallic nanoparticles, with applications in sensing, detection, and imaging [1,2]. The development of new procedures for the manufacture of functional silver nanoparticles and their use in bio sensitization is now an important research area in the field of research [3]. Fabrication processes of silver nanoparticles are constantly improving, and allowing for greater control over their size and structure. Silver nanoparticles are utilized to improve white light photoluminescence and are an interesting contender for therapeutic, diagnostic, and photo thermal drug delivery applications [4,5]. The Ag NPs are utilized in biomedical applications, cellular imaging, molecular diagnosis, targeted therapy, and as contrast agents, photo thermal agents, and radio sensitizers, as well as in contrast agents, photo thermal agents, and radio sensitizers [6-8]. In addition to their structure, composite, and shape, their usefulness is due to their stability and unusual optical, electrical, magnetic, oxidation resistance, and structural features [9]. Noble metal nanoparticles, such as Ag NPs, have been a source of great interest to their unusual physical features, particularly their strong Plasmon absorption peak in the visible region [10]. The resonance frequencies are determined by particle form and size and remain stable for months [11].

Diverse methods related to developing silver nanoparticles such as ultrasonic irradiation, electrochemical synthesis, thermal decomposition, radiolysis, and the chemical reduction of metal salts have been reported [12-16]. The chemical reduction method can be considered as one of the most important and most popular preparation technique for preparing Ag and Au colloids [17].

In the present study, we have synthesized silver nanoparticles from silver nitrate salt solution with trisodium citrate as the reducing agent.

This approach allows for regulated particle size and form by varying the molar concentration of reactants. Metal salt precursor, reducing agent, and stabilizing/surfactants/capping agent are the three key components used in this procedure. The two stages of the silver reduction process are nucleation and particle growth [18]. When compared to the physical approach, the chemical method has the following advantages: high yield, cost-effective production, and easy particle size control [19]. Despite numerous attempts, preparing Ag NPs with a well-defined size remains difficult, necessitating a second procedure to prevent particle aggregation [20]. Synthesis of Ag

NPs utilizing stabilizers, surfactants, and capping agents has been evaluated and reported to prevent aggregation [21,22].

Sol-gel materials are inorganic/organic hybrid materials made by combining a metal alkoxide and an organic alkoxysilane precursor with water and a solvent in the presence of an acid or base catalyst to hydrolyze and condense [23].

It can form highly porous rigid membranes, which can be designed to trap/immobilize biomolecules such as enzymes and proteins that retain their biological function with potential fouling release function, as well as for other applications [24]. The effect of using different precursors and a range of mixing times for sol-gel formulations on the ability of the coatings to inhibit macrofouling has been found [25,26]. In this study, silica network, which provided a matrix for introducing Ag NPs, were prepared to demonstrate their role in filling the pores of the silica sol-gel network to increase the absorbance of the SPR bands. In our subsequent study, Ag NPs within a silica sol gel network (as a catalyst) are used to enhance the white light photoluminescence after using the rare earth elements.

2. Experimental Part

Without further purification, silver nitrate ($AgNO_3$) (purity >98%) and trisodium citrate ($C_6H_5O_7Na_3$) (purity 99%) were utilized as starting materials. According to Lee and Meisel [27], the silver colloid was synthesized utilizing the chemical reduction approach. All reactive material solutions were made with distilled water.

A 62.5 mL of $AgNO_3$ solution was heated to boiling in a typical experiment. Drop by drop, 2.5 mL was added of 5% trisodium citrate to this solution. The solution was forcefully stirred during the operation. The solution was heated until the color changed (pale yellow) (Fig. 1). Then it was taken off the heating element and stirred until it reached room temperature.

Mechanism of reaction could be expressed as follows:

$$4Ag^{+} + C_6H_5O_7Na_3 + 2H_2O \rightarrow 4Ag^{0} + C_6H_5O_7H_3 + 3Na + O_2 + H$$

To prepare a suitable transparent host of Ag, pure silica xerogel sol-gel rod samples were prepared under certain reaction conditions. In a 1:5:10 volume ratio, pH 1.5, TEOS and absolute EthOH were mixed together. Before the hydrolysis, a 1ml Ag NPs solution with various Ag concentrations was added to the combination of TEOS and EthOH and indicated as sol(I), which was then homogenized for 15 min. under magnetic stirrer. Then mixture 0.6 mL deionized water and 1.2 mL absolute EthOH to the solution. This combination was labeled sol(Π) and added slowly to the sol(I) for hydrolysis. The resulting solution was stirred for 30 minutes with a magnetic stirrer before adding 0.5 ml of N,N-dimethylformamide. The resulting solution was placed into a sealed glass tube and held below the reaction temperature of 80°C. After aging and drying, the xerogel bulk rod samples were sintered at 250°C by gradually increasing the temperature from 110 to 250°C during 48 hours.

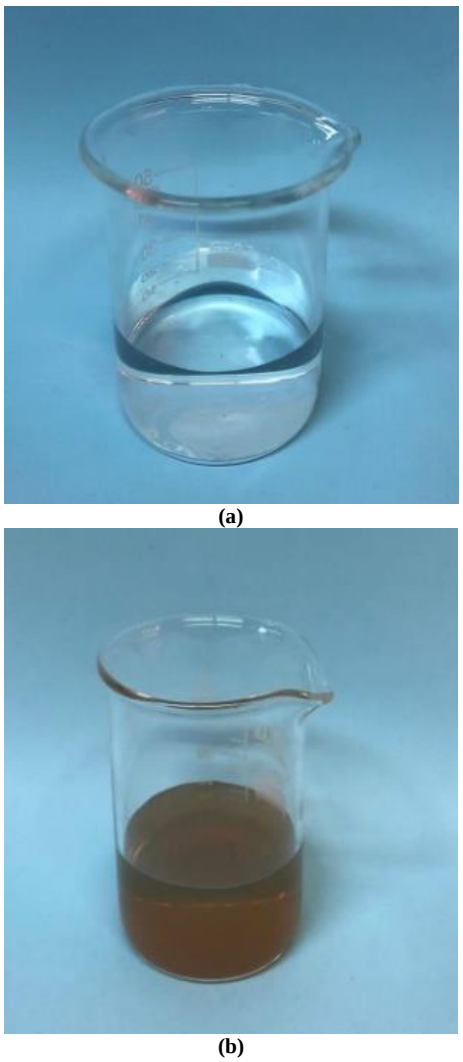

(a) **(b)**

Fig. (1) (a) $AgNO_3$ solution and (b) Ag NPs

3. Results and Discussion

In order to explore the influence of these preparations on characterization of such nanostructures, the absorption of Ag colloidal was recorded as a function of $AgNO_3$ concentration and reduction period. Figure (2) depicts the absorption spectra of Ag colloidal produced at various reduction durations of heating after boiling point and with various $AgNO_3$ concentrations. At first glance, the absorbance increases as the heating duration increases, while at molar concentration of $2.0x10^{-3}$M, the SPR band at approximately 407.1 nm is generated at 9 minutes after the boiling point (Fig. 2a), and at $3.0x10^{-3}$M (7 min.) at wavelengths 416.12 nm.

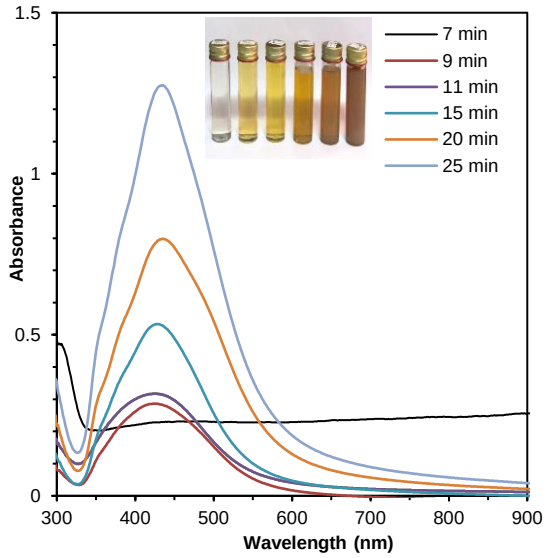

(a)

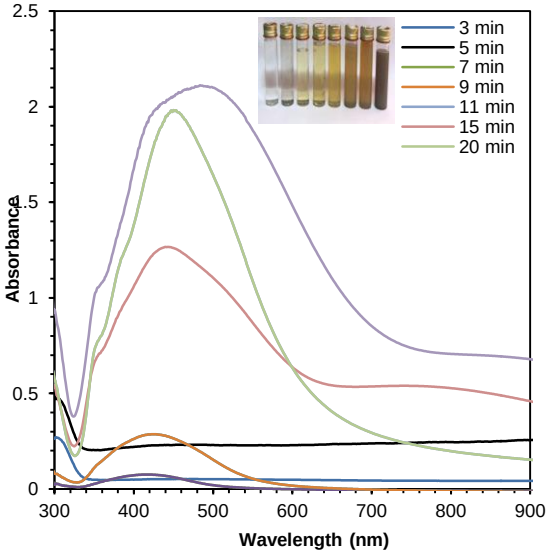

(b)

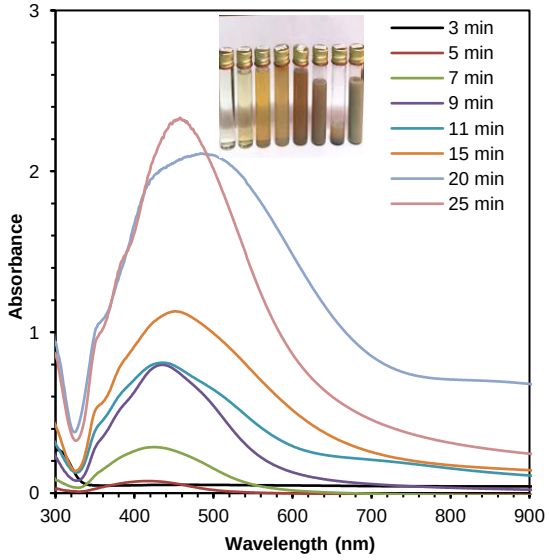

(c)

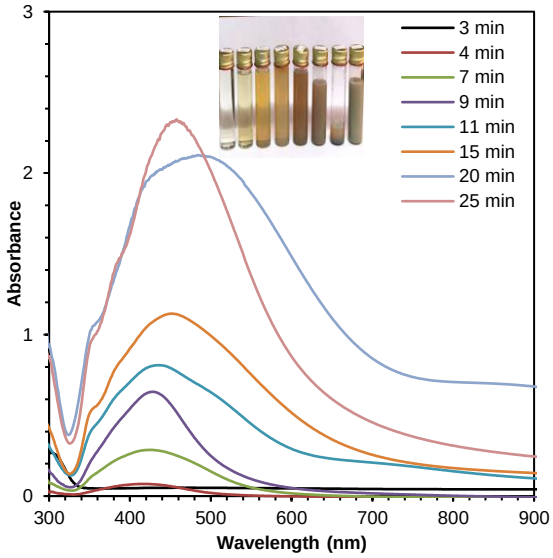

(d)

Fig. (2) Absorption spectra of Ag colloidal samples prepared by chemical reduction method at different reduction periods and different concentrations: (a) 2.0x10^{-3}M, (b) 3.0x10^{-3}M, (c) 4.0x10^{-3}M, and (d) 5.0x10^{-3}M

Figures (2c) and (2d) at the two concentrations of 4.0x10^{-3}M and 5.0x10^{-3}M at (5 and 4 min.) at wavelengths 409.05 and 406.02 nm, respectively. This suggests that the overall pattern of peak absorption for silver nanoparticles as a function of reduction periods is "red shift", which can be explained by increased Ag NPs concentration through aggregation formation as the reduction time increases. There is no evidence of the occurrence of a SPR band at low concentrations (1.0x10^{-3}M and 1.0x10^{-4}M).

The absorbance as a function of reduction period is shown in Fig. (3). The absorbance increased as the reduction period grew, indicating that as the reduction time increased, nanoparticles aggregation occurred, resulting in an increase in Ag NPs concentration, and thus the absorbance increased, which is consistent with Beer-Lambert laws.

The particle size of produced Ag NPs is estimated using the FE-SEM equipment. Initially, colloidal silver nanoparticles were deposited on glass microscope slides using the drop casing method. From the first glance to the FE-SEM shot of the Ag NPs prepared by varying the concentration, one can see a homogeneous distribution of Ag NPs in the shape of nanosphere particles with particle sizes ranging from nano to nanoscale (15-33nm) as shown in Fig. (4).

It is obvious that when the reduction period is short, the particle size is smaller than when the reduction period is long, and this is correlated with the color of silver colloidal at light yellow, which indicates a small particle size, but more color toward the dark yellow liquid down to brown indicates a larger particle size with a higher probability of aggregation formation.

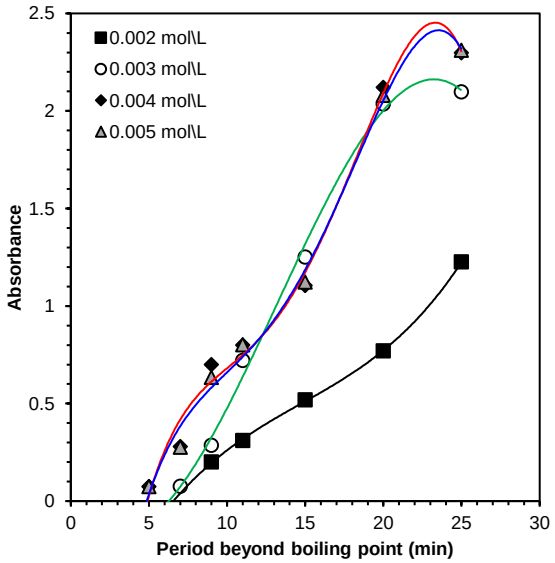

Fig. (3) Variation of absorbance with reduction periods for different concentration of Ag NPs synthesized by chemical reduction method

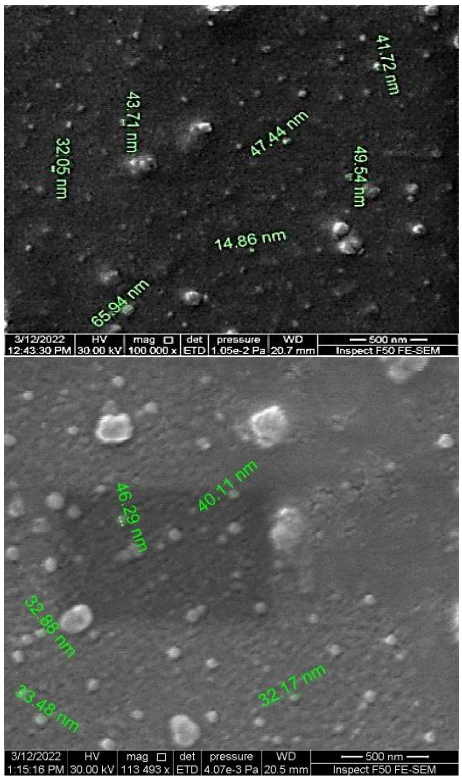

Fig. (4) FE-SEM images of Ag NPs synthesized after different reduction periods beyond boiling

The phase structure of synthesized Ag NPs was studied by recording the XRD pattern of one of the generated samples using a copper x-ray diffractometer (see Fig. 5). It can be seen that the diffraction peaks at 2θ equal to 32°. Liquid colloidal Ag NPs must be included into a solid host such as polymer or sol-gel host to prevent breakdown by caging it into a solid network, however Ag NPs stability in liquid phase is a global challenge.

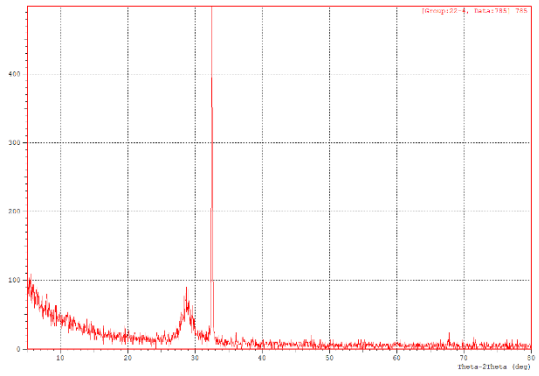

Fig. (5) XRD pattern of Ag NPs synthesized after 5 min. reduction period and 5.0x10^{-3} mol\L concentration

To improve the absorbance of silica xerogel, a dopant of Ag NPs was added. The purpose of this section is to explain how silver affects the absorption spectra of Ag NPs solution and pure silica xerogel samples, and gives us a simplest insight about the silver's behavior in silica network.

The absorption coefficient vs. wavelength of silica xerogels doped with different amounts of Ag NPs is shown in Fig. (6). After identifying the optimum particle size conditions, it can be seen that the absorption coefficient α(λ), at the peak of each band, increases somewhat with increasing Ag NPs concentration.

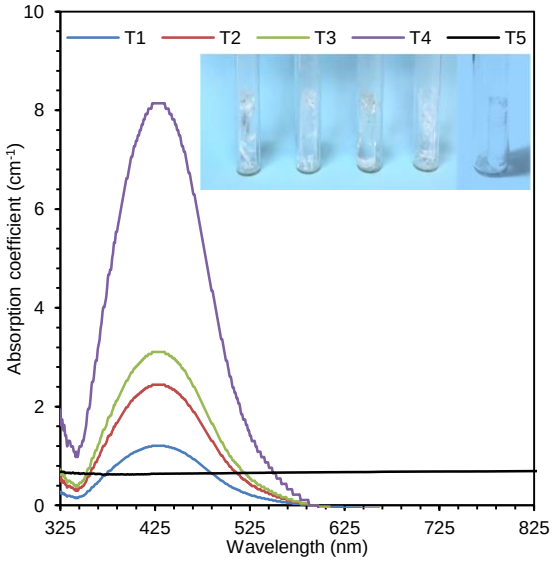

Fig. (6) Absorption spectra of silica xerogel doped with different concentrations of Ag NPs: T1 = 2.0x10^{-3}M, T2 = 3.0x10^{-3}M, T3 = 4.0x10^{-3}M, T4 = 5.0x10^{-3}M, and T5 = silica xerogel (after 9 min reduction period)

The characteristic vibrational bands of silica were found in the FTIR spectra of silica xerogel sample and silica xerogel doped with Ag NPs, as shown in Fig. (7), which were prepared under synthetic recipe conditions of pH 1.5, 1:5:10 volume ratio and temperature of 80°C, dried at 110°C and sintered at 250°C, and Ag NPs synthesized at 5 min. reduction

period and $0.5x10^{-3}$ mol/L concentration. The bending vibrations of Si-O-Si groups cause the absorption band centered at 460.2 cm^{-1}, the symmetric stretching Si-O-Si groups cause the absorption band peaking at 810.1 cm^{-1}, and the wide band around 1103.8 cm^{-1} is the distinctive Si-O-Si asymmetric stretching vibrations. The weak band at 964.8 cm^{-1}, attributed to stretching vibrations of silanol (Si-OH) groups, suggests that there are just a limited number of these groups in the silica network, implying that the condensation reaction is practically complete. Because the water molecules in the pores of silica xerogel were not entirely trapped throughout the drying process at 110°C, two absorption bands appeared. The first band, which peaks at 1640.7 cm^{-1}, is caused by bending vibrations of the O-H bond in H_2O molecules, whereas the second band, which peaks at 3440 cm^{-1}, is caused by stretching vibrations of the link. For the pure glass sample sintered at 250°C, however, the first band became very weak and the second band vanished, indicating that the majority of H_2O molecules are driven out following the sintering process.

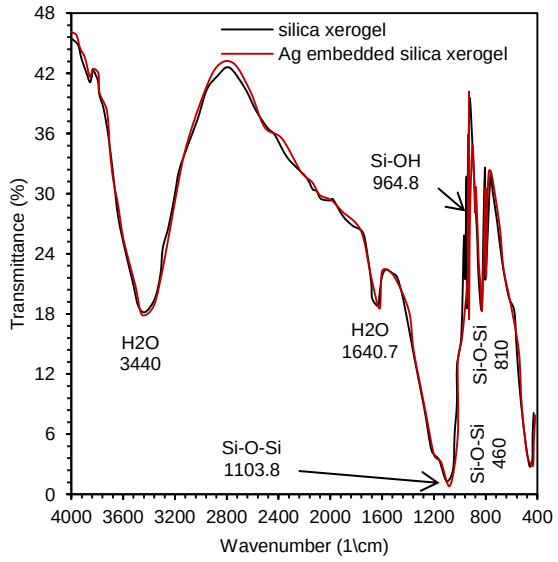

Fig. (7) FTIR transmission spectra of silica xerogel and silica xerogel doped with Ag NPs

From the XRD patterns shown in Fig. (8), it is clear that the presence of Ag NPs inside the silica xerogel did not affect the random behavior of silica despite its crystal phase, because the doping rate is part of million. Also, Ag NPs are located inside the pores and do not associate with the structural network, so it does not affect the random behavior of silica.

4. Conclusions

In concluding remarks, it was shown that the chemical stability of Ag NPs synthesized by chemical reduction method at short reduction period after boiling is higher than that of Ag NPs synthesized at long reduction period after boiling. As well, smaller and uniform distribution of Ag NPs can be obtained by using short period of reduction. At low concentrations ($<10^{-3}$M), the SPR was not observed.

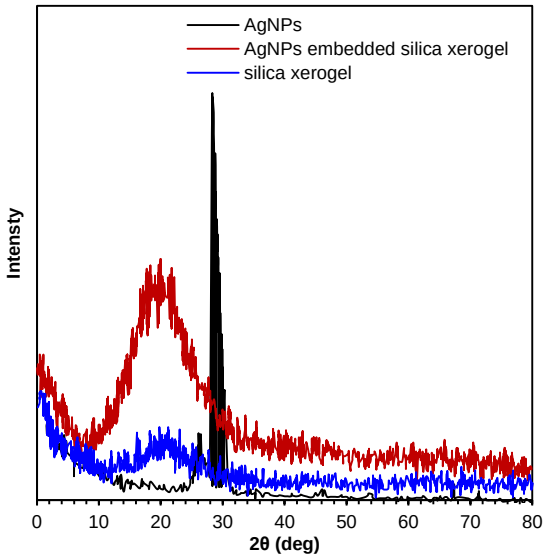

Fig. (8) XRD patterns of Ag NPs, silica xerogel, and Ag NPs embedded in silica xerogel

References

[1] I. Khan, K. Saeed and I. Khan, "Nanoparticles: Properties, applications and toxicities", Arab. J. Chem., 12(7) (2019) 908-931.
[2] S. Smonia Joe Princy et al., "Detection of heavy metals, SERS and antibacterial activity of polyvinylpyrolidone modified plasmonic nanoparticles", Enviro. Res., 210 (2022) 112883.
[3] S.F. Ahmed et al., "Green approaches in synthesising nanomaterials for environmental nanobioremediation: Technological advancements, applications, benefits and challenges", Enviro. Res., 204A (2022) 111967.
[4] C. Caro et al., "Silver nanoparticles: sensing and imaging applications", INTECH, 65(51) (2010) 202-224.
[5] B.T. Chiad et al., "Study the optimum conditions of synthesis Ag NPs by chemical reduction method", J. Kerbala Univ., 11(4) (2013) 40-46.
[6] S. Liu et al., "Anti-RhoJ antibody functionalized Au@I nanoparticles as CT-guided tumor vessel-targeting radiosensitizers in patient-derived tumor xenograft model", Biomater., 141 (2017) 1-12.
[7] C. Gomez et al., "Medical Applications of Metallic Bismuth Nanoparticles", Pharmaceutics, 13(11) (2021) 1793.
[8] C. Ji et al., "Biocompatible Tantalum Nanoparticles as Radiosensitizers for Enhancing Therapy Efficacy in Primary Tumor and Metastatic Sentinel Lymph Nodes", ACS Nano, 16(6) (2022) 9428-9441.
[9] K.-C. Lee et al., "Size effect of Ag nanoparticles on surface plasmon resonance", Surf. Coat. Technol., 202 (2008) 5339-5342.

[10] J.K. Majhi and P.K. Kuiri, "Enhancement of spectral shift of plasmon resonances in bimetallic noble metal nanoparticles in core–shell structure", J. Nanopart. Res., (22) (2020) 546-551.
[11] A. Moores and F. Goettmann, "The plasmon band in noble metal nanoparticles: an introduction to theory and applications", New J. Chem., 30(8) (2006) 1121-1132.
[12] A. Pyatenko, M. Yamaguchi and M. Suzuki, "Synthesis of Spherical Silver Nanoparticles with Controllable Sizes in Aqueous Solutions", J. Phys. Chem. C, 111(2) (2007) 7910-7917.
[13] K.M.M.A. El-nour, A. Al-warthan and R.A.A. Ammar, "Synthesis and application of silver nanoparticles", Arab. J. Chem., 3(3) (2010) 135-140.
[14] T. Ghodselahi, T. Neishaboory and M.A. Vesaghi, "Localized surface plasmon resonance of Cu_2O core shell nanoparticles: absorption scattering and luminescence", Biosensors, 2 (2011) 59-61.
[15] Q.H. Tran, V.Q. Nguyen and A. Le, "Silver nanoparticles: synthesis, properties, toxicology, applications and perspectives", Adv. Nat. Sci.: Nanosci. Nanotechnol., 4 (2013) 1-20.
[16] L. Mahmudin et al., "The effect of the concentration of the stabilizer in the formation of a silver nanoparticle on the phenomenon of Surface Plasmon Resonance (SPR) as an active material for biosensor", J. Phys.: Conf. Ser., (2021) 1763-12064.
[17] J. Natsuki, T. Natsuki and Y. Hashimoto, "A Review of Silver Nanoparticles: Synthesis Methods, Properties and Applications", Int. J. Mater. Sci. Appl., 4(5) (2015) 325-332.
[18] T.K. Nguyen et al., "Mechanisms of Nucleation and Growth of Nanoparticles in Solution", Chem. Rev., 114(15) (2014) 7610-7630.
[19] N. Baig, I. Kammakakam and W. Falath, "Nanomaterials: a review of synthesis methods, properties, recent progress, and challenges", Mater. Adv., 2 (2021) 1821-1871.
[20] M. Zahoor et al., "A Review on Silver Nanoparticles: Classification, Various Methods of Synthesis, and Their Potential Roles in Biomedical Applications and Water Treatment", Water, 13(16) (2021) 2216.
[21] A. Syafiuddin et al., "A Review of Silver Nanoparticles: Research Trends, Global Consumption, Synthesis, Properties, and Future Challenges", J. Chin. Chem. Soc., 64 (2017) 732-756.
[22] M.Z. Hossain et al., "Synthesis of Spherical Silver Nanoparticles by Chemical Reduction Method", J. Bangladesh Chem. Soc., 30(20) (2021) 42-47.
[23] J.Y. Wen and G.L. Wilkes, "Organic/inorganic hybrid network materials by the sol–gel approach", Chem. Mater., 8 (1996) 1667-1681.
[24] S. Smith et al., "A Comprehensive Review of the Covalent Immobilization of Biomolecules onto Electrospun Nanofibers", Nanometr., 10 (2020) 2142.
[25] Y. Tang et al., "Hybrid xerogel films as novel coatings for antifouling and fouling release", Biofouling, 21 (2005) 59-71.
[26] L. Mahmudin et al., "The effect of the concentration of the stabilizer in the formation of a silver nanoparticle on the Resonance (SPR) as an active material for biosensor", J. Phys.: Conf. Ser. (2021) 1763-012064.
[27] J. Fang, C. Zhong and R. Mu, "The Study of Deposited Silver Particulate Films by Simple Method for Efficient SERS", Chem. Phys. Lett., 401 (2005) 271-275.

IRAQI JOURNAL OF APPLIED PHYSICS
Vol. 18, No. 3, July-September 2022, pp. 31-34

Zeena J. Raheem

Department of Physics, College of Education, Al-Iraqia University, Baghdad, IRAQ

Determination of Uranium and Thorium levels and Measurement of Annual Effective Dose levels in Some Canned Foods

In this study, the technique of nuclear trace detectors was used to measure the levels of uranium-thorium concentrations in some samples of canned meat and fish. Sixteen samples were collected from the local markets of Baghdad - Iraq. It was found that the levels of thorium concentrations are higher than the levels of uranium concentrations in all canned meat and fish samples. It was also found that the average annual effective dose of uranium and thorium in canned meat samples is higher than the average annual effective dose in canned fish samples. When comparing the practical results with the internationally permissible results, it was found that the levels of uranium and thorium concentrations of the studied samples are within the permissible limits.

Keywords: Canned food; Uranium concentration; Thorium concentration; Trace detector
Received: 05 July 2022; Revised: 01 August 2022; Accepted: 08 August 2022

1. Introduction

Food of animal origin is among the many products that provide many important nutrients. Canned products have a long shelf life and do not need to be kept at low temperatures, nor do they require special handling during transportation or distribution processes [1]. Some chemical preservatives such as sodium nitrate or potassium nitrate are often added to canned foods [2].

The levels of radionuclides in foods vary and depend on several factors. Among these factors are the type of food and the geographical area in which these substances were produced, and the common radionuclides in foodstuffs are potassium (K), radium (Ra), thorium, and uranium [3].

Uranium is found in a variety of foodstuffs. The highest concentrations are found in shellfish, and smaller amounts have been measured in fresh vegetables, grains, and fish [4]. Uranium travels rapidly in the bloodstream because it binds primarily to red blood cells. Although uranium is a non-essential component of the environment, when it accumulates in people, it has chemical and radioactive effects that can pose a number of health risks. The kidneys, liver, and bones are the main locations where uranium builds up in the human body. The main uranium-related chemical consequence in people is nephritis. The route of exposure, particle solubility, contact time, and route of elimination all affect how hazardous uranium is. Uranium is transported, absorbed, and ultimately may accumulate in body organs and tissues in the form of uranyl ions in bodily fluids. Numerous health organizations worldwide are keeping an eye on the amounts of radionuclides like uranium to see if they are within the allowable limit due to the hazardous consequences they bring [5]. the permissible limit of uranium given by ICRP (2012) is 1 mSv/year [6].

The use of Solid State Nuclear Track Detectors (SSNTD) has become well-known and has been used in a number of fields, including earth sciences, micro-pore membrane technology, nuclear physics, dosimetry, and radiography. The concentrations of uranium and thorium in a variety of samples, including soil, water, tissues, and biological components, are easily determined using these reagents. It is well known that solid-state nuclear pathway detectors have advantages over other detectors due to their long-term trace retention, ease of use, relatively low cost, and ability to calculate the alpha track without the use of special electronics. They also have high sensitivity to heavy charged particles from nuclear radiation by collecting traces for a long time and are not affected by various environmental factors like heat, humidity, or light [7].

In general, canned fish and meat make up a large part of the food market in the country. Despite its flavor and nutritional benefits, canned foods may contain chemical contaminants. The environment is the primary source of these pollutants, and improper technological treatment or poor packaging may contribute to the pollution [3]. The purpose of this work is to determine the levels of uranium and thorium in canned foods made with ingredients derived from animals to determine whether they are within the allowed limits internationally. In addition, the health risks associated with the consumption of this particular group of products have been identified.

2. The materials and methods used

Collection of Samples

For the purpose of measuring the concentrations of radioactive uranium and thorium, sixteen samples were collected from different types of canned fish and meat from local markets in Baghdad, Iraq. Tables were made for meat and fish samples according to the

name of the sample and the country of origin, as well as dividing the samples into two groups, the group of canned meat and the group of canned fish, as in Table (1) and (2).

Table (1) Name and origin of canned meat samples

Sample code	Trademark	Origin
M1	ALTaghziah, Beef luncheon meat	Lebanon
M2	ALTaghziah, Chicken luncheon meat	Lebanon
M3	Hana , Beef luncheon meat	UAE
M4	Hana Chicken luncheon meat	UAE
M5	Tazaj beef luncheon meat	Iraq
M6	Tazaj Chicken luncheon meat	Iraq
M7	Zwan beef luncheon meat	Netherland
M8	Zwan Chicken Luncheon Meat	Netherland

Table (2) Name and origin of canned fish samples

Sample code	Trademark	Origin
F1	Al Alali , fancy sardines	Saudi Arabia
F2	Milo , sardines in vegetable oil	Morocco
F3	SIFA , sardines in vegetable oil	Morocco
F4	Bella, sardines in vegetable oil	Indonesia
F5	Sardines Rio Mare	Thailand
F6	Goody light tuna	Saudi Arabia
F7	tuna Rio Mare	Italy
F8	Botan ,light meet tuna	USA

Sample preparation

To measure uranium and thorium concentrations in canned meat and fish samples, the samples were dried for dehumidification by placing them in an oven for 24 hours at 250°C. After drying, the samples were ground and sieved with a clamp with a hole diameter of 1 mm to obtain homogeneous samples. Then, chips were prepared from nuclear tracer reagent (CR-39) with the approximate area, with samples of canned meat and fish, weighing (0.5 g). The powder samples, after mixing them with certain proportions of starch, were pressed into a disk of the thickness (1.5 mm) and diameter (13 mm) using a piston with a pressing force of up to (15 tons).

Neutron Irradiation method

The neutron activation method was used to measure the concentrations of uranium and thorium in samples of canned meat and fish, as well as for standard samples. The sample discs were placed in contact with a trace detector (CR-39) in paraffin wax as a moderator at a distance (5 cm) from the neutron source (^{241}Am-Be) with a neutron flux to obtain thermal neutrons as in Fig. (1) The irradiation period was seven days, and therefore the samples were exposed to a flood of thermal neutrons, and through the nuclear reaction [8], the effects of nuclear fission fragments were recorded in the detector as [9]

$$^{9}_{5}Be + {}^{4}_{2}He \rightarrow {}^{12}_{6}C + {}^{1}_{0}n + 5.76\ MeV \qquad (1)$$

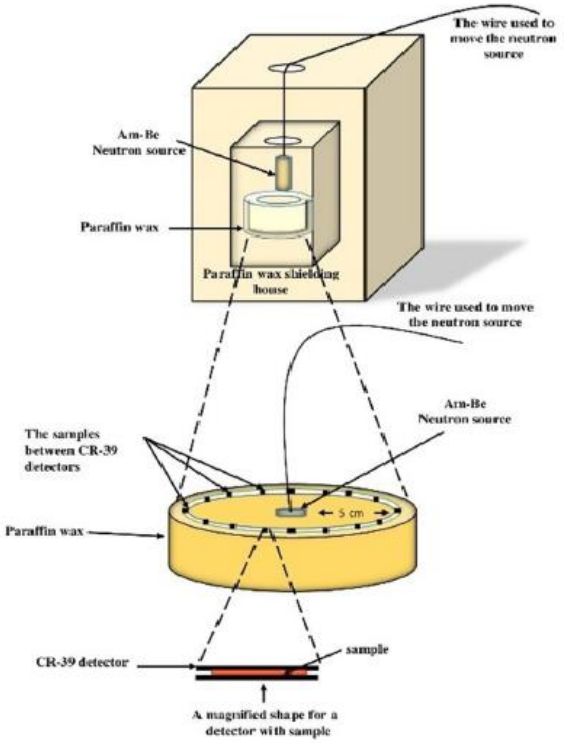

Fig. (2) Schematic diagram of irradiation of detectors and samples with neutron source [6]

Then the reagents were taken after the irradiation period and chemical scraping was performed on them using a solution of sodium hydroxide NaOH with a caliber of 6.25N at a temperature of 60°C for four hours, then the reagents were washed and dried, and the density of the traces was calculated using an optical microscope with a magnification of 400X. The concentrations of uranium isotopes were calculated using the following equation [10]:

$$C^{U}_{Samples} = \frac{C^{U}_{Calibration} \cdot \rho_{Sample.\varepsilon}}{\rho_{calibration} \cdot R_{eff}} \qquad (2)$$

where, ρ_{Sample} and $\rho_{calibration}$ are the density of tracks per cm^{-2} in detector for sediment and standards, respectively. ε is the etching efficiency and R_{eff} is the effective range [7].

Thorium concentrations in canned fish and meat samples were calculated using the following equation

$$\rho_U + \rho_{Th} = K_U . C_U (1 + \frac{K_{Th} . C_{Th}}{K_U . C_U}) \qquad (3)$$

where, ρ_U and ρ_{Th} are the track densities on the detector of U and Th series, respectively. C_U and $C_{Th}$are the concentrations of U and Th in the sample. K_U and K_{Th} are α registration efficiency from U and Th series,respectively and were determined by using standard sources, where, $\rho_U + \rho_{Th}$ is the total track density on CR-39 detector in Eq. (3), if the uranium concentration is known, the thorium concentration can be calculated [7].

Calculation of committed effective dose

The total committed effective dose due to ingestion of radionuclides in canned fish and meat,

for a given age group, can be determined using the following equation [11]

$Dose_{EFj} = \sum_{ik}(DC_{ij} \times R_{jk} \times C_{ik} \times 1000)$ (4)

where $Dose_{EFj}$ is the committed effective dose (mSv/year) due to ingestion of radioactive uranium and thorium found in canned fish and meat of age group (j) [11].

In this study, the adult age group was selected, with limits greater than 18 years, according to what was published by the International Commission on Radiological Protection (ICRP). DC_{ij} is the ingestion dose coefficient (Sv/Bq) for radionuclide (i) for each age group (j).

The International Commission on Radiological Protection (ICRP) has published dose coefficients for each radionuclide which take into account the sensitivity of organs and tissues in the body, the biological half-life of the radionuclide and the type of radiation emitted [6].

R_{jk} is the consumption rate (kg/year) for the age group (j) for food type (k)

C_{ik} is the activity concentration of the radionuclide in the food (Bq/kg) for radionuclide (i) and food type (k) [11].

3. Result and discussions

Table (3) shows the results of radioactive uranium and thorium concentrations in canned meat samples available in the local markets in Iraq. It is noted that the highest concentration of uranium in the sample (M8) and the level of concentration (3.502±0.013 Bq/kg) and the lowest concentration level in the sample (M1) and the level of concentration (0.634±0.123 Bq/kg). As for the results of thorium concentrations, they were higher than uranium concentrations, the highest concentration level (13.760±1.987 Bq/kg) in the sample (M7) and the lowest concentration level (2.897±0.0238 Bq/kg) in the sample (M8).

Table (3) Concentrations of uranium and thorium in canned meat samples

Sample code	^{238}U Bq/kg	^{232}Th Bq/kg
M1	0.634±0.123	6.894±1.234
M2	1.450±0.023	4.876±0.873
M3	3.125±0.02	10.234±1.349
M4	2.813±0.191	2.987±0.235
M5	1.967±0.106	7.345±1.986
M6	0.946±0.0876	5.872±0.981
M7	2.456±0.0230	13.760±1.987
M8	3.502±0.013	2.897±0.0238

Table (4) shows the concentration levels of radioactive uranium and thorium in canned fish samples. It is noted that the highest concentration of uranium in the sample (F5) and the level of concentration (3.905±1.098 Bq/kg) and the lowest concentration level in the sample (F4) and the level of concentration (0.987+0.546). As for the results of thorium concentrations, they were higher than uranium concentrations, the highest concentration level (15.098±1.98 Bq/kg) in the sample (F4) and the lowest concentration level (3.832±0.987 Bq/kg) in the sample (F3).

Table (4): Concentrations of uranium and thorium in canned fish samples

Sample code	^{238}U Bq/kg	^{232}Th Bq/kg
F1	1.981±1.023	7.980±1.034
F2	2.980±0.450	5.678±0.987
F3	1.987±0.098	3.832±0.987
F4	0.987+0.546	15.098±1.98
F5	3.905±1.098	12.324±2.89
F6	1.98+0.453	9.546±2.98
F7	3.786±1.034	5.986+0.234
F8	1.980±0.094	4.989±1.988

Effective doses for canned fish and meat were calculated for the adult age group and are shown in Tables (5) and (6). The reference level for exposure is 1 mSv/year [6], and it was noted in both tables that the equivalent dose rate from eating canned fish and meat is within the internationally permissible limits.

Table (5) the effective annual dose of uranium and thorium in canned meat samples

Sample code	^{238}U mSv/year	^{232}Th mSv/year
M1	0.0014265	0.079281
M2	0.0032625	0.056074
M3	0.00703125	0.117691
M4	0.00632925	0.0343505
M5	0.00442575	0.0844675
M6	0.0021285	0.067528
M7	0.005526	0.15824
M8	0.0078795	0.0333155
Average	0.004751	0.078868

Table (6) Effective annual dose of uranium and thorium in canned fish samples

Sample code	^{238}U mSv/year	^{232}Th mSv/year
F1	1.34E-03	0.027531
F2	2.01E-03	0.0195891
F3	1.34E-03	0.0132204
F4	6.66E-04	0.0520881
F5	2.64E-03	0.0425178
F6	1.34E-03	0.0329337
F7	2.56E-03	0.0206517
F8	1.34E-03	0.01721205
Average	1.65E-03	0.028217981

It is noticed in figures (2) and (3) that the average effective annual dose of uranium and thorium in canned meat samples is greater than the average effective annual dose of uranium and thorium in canned fish samples.

After reviewing the results, we found that additional research is required to determine the amount of radioactive uranium and thorium in dietary staples that may harm human health. Since evidence on the consequences of poisoning may take a long time to manifest, the current state of knowledge does

not permit a categorical declaration that the accepted toxicological standards are accurate. However, according to these results, one may conclude that the concentration levels of uranium and thorium in the canned foods, mainly fish and meat, in the local markets of Baghdad city are not hazardous to the people health.

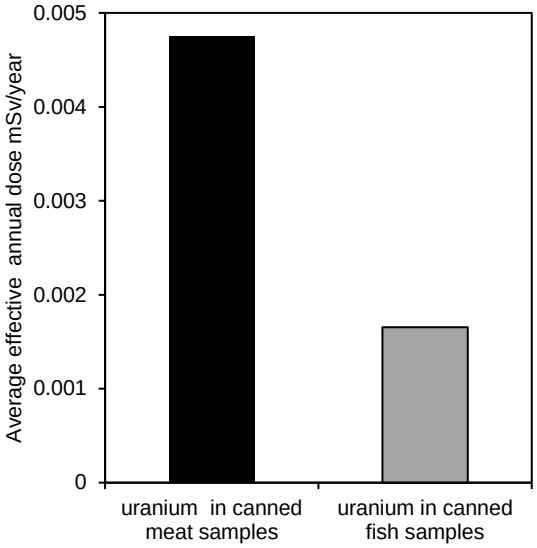

Fig. (2) Comparison between the average annual effective dose of uranium in canned meat and canned fish samples

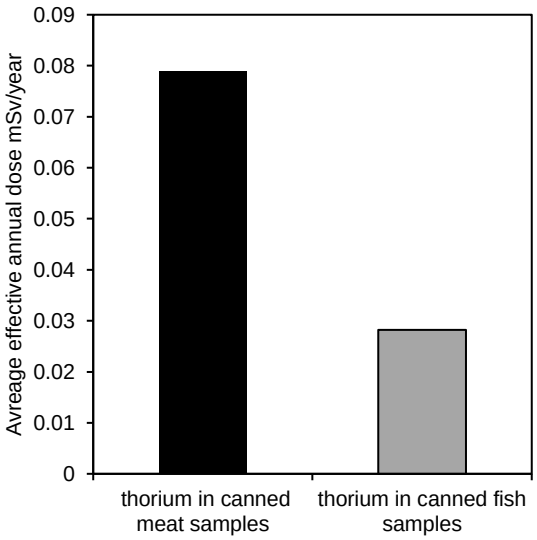

Fig. (3) Comparison between the average annual effective dose of thorium in canned meat and canned fish samples

4. Conclusions

In concluding remarks, it was found that the average annual effective dose of uranium and thorium in canned meat samples is higher than the average annual effective dose in canned fish samples. Also, it was found that thorium concentration levels are higher than uranium concentration levels in all canned meat and fish samples. All samples of canned meat and fish are considered radiologically safe. The levels of uranium and thorium concentrations are within the internationally permissible limits.

References

[1] M. Pateiro et al., "Application of essential oils as antimicrobial agents against spoilage and pathogenic microorganisms in meat products", Int. J. Food Microbiol., 337 (2021) 108966.
[2] S.K. Amit et al., "A review on mechanisms and commercial aspects of food preservation and processing", Agric. Food Secur., 6.1 (2017) 1-22.
[3] G. Kowalska, U. Pankiewicz and R. Kowalski, "Determination of the level of selected elements in canned meat and fish and risk assessment for consumer health", J. Anal. Meth. Chem., 2020, Article ID 2148794.
[4] R. Engelbrecht, "Environmental radioactivity monitoring. In Handbook of Radioactivity Analysis", vol. 2 (Academic Press, 2020) 1-40.
[5] T. Sharma et al., "Uranium distribution in groundwater and assessment of age dependent radiation dose in Amritsar, Gurdaspur and Pathankot districts of Punjab, India", Chemosphere, 219 (2019) 607-616.
[6] ICRP, 2012, Compendium of Dose Coefficients based on ICRP Publication 60. ICRP Publication 119. Anna. ICRP 41 (Suppl.).
[7] P. Otansev and E. Nizamettin, "Determination of uranium and thorium concentrations in sediment samples by using solid state nuclear track detectors", Appl. Rad. Isotop. 172 (2021) 109652.
[8] R.S. Ahmed et al., "Evaluation of uranium concentration in the blood breast cancer women with CR-39 detector", Appl. Rad. Isotop., 182 (2022) 110120.
[9] W.N. Raja and Z.J. Raheem, "Determination of Uranium concentrations in Soil samples of Al-Tarmiya using the track detector CR-39", J. Edu. Sci. Stud., 1(1) (2013).
[10] M.G. Al-Gharabi and A.A. Al-Hamzawi, "Investigation of uranium concentrations in selected soil samples of Al-Diwaniyah governorate, Iraq using CR-39 detector", J. Phys.: Conf. Ser., 1234(1) (2019) 012061.
[11] S. Sdraulig et al. Radiation doses from the average Australian diet. No. TR--181. Australian Radiation Protection and Nuclear Safety Agency (ARPANSA), 2019.

THE IRAQI JOURNAL OF APPLIED PHYSICS
EDITORIAL BOARD

COPYRIGHT RELEASE FORM
IRAQI JOURNAL OF APPLIED PHYSICS (IJAP)

We, the undersigned, the author/authors of the article titled

……
……
……
……
……
……
……

that is submitted to the Iraqi Journal of Applied Physics (IJAP) for publication, declare that we have neither taken part or full text from any published work by others, nor presented or published it elsewhere in any other journal. We also declare transferring copyrights and conduct of this article to the Iraqi Journal of Applied Physics (IJAP) after accepting it for publication.

The authors will keep the following rights:

1. Possession of the article such as patent rights.
2. Free of charge use of the article or part of it in any future work by the authors such as books and lecture notes after informing IJAP editorial board.
3. Republishing the article for any personal purposes of the authors after taking journal permission.

To be signed by all authors:

Signature:……..date: ……
Printed name: ……

Signature:……..date: ……
Printed name: ……

Signature:……..date: ……
Printed name: ……

Correspondence
address:……...
……
Address:……
……
Telephone:……..……..email: ……

Note: Complete and sign this form and mail it to the below address with your finally revised manuscript

The Iraqi Journal of Applied Physics
www.iraqiphysicsjournal.com
Email: info@iraqiphysicsjournal.com
Email: editor_ijap@yahoo.co.uk
Email: ijap.editor@gmail.com

IRAQI JOURNAL OF APPLIED PHYSICS

Volume (18) Issue (3) July-September 2022

CONTENTS